Higher-order topological phases emerging from Su-Schrieffer-Heeger stacking

Xun-Jiang Luo,[1,2] Xiao-Hong Pan,[2,3] Chao-Xing Liu,[4] and Xin Liu[2,3,*]

[1]*School of Physics and Technology, Wuhan University, Wuhan 430072, China*

[2]*School of Physics and Institute for Quantum Science and Engineering, Huazhong University of Science and Technology, Wuhan, Hubei 430074, China*

[3]*Wuhan Institute of Quantum Technology and Hubei Key Laboratory of Gravitation and Quantum Physics, Wuhan, Hubei 430074, China*

[4]*Department of Physics, the Pennsylvania State University, University Park, Pennsylvania 16802, USA*

(Received 8 March 2022; revised 30 November 2022; accepted 15 December 2022; published 13 January 2023)

In this work, we develop a systematic approach of constructing and classifying the model Hamiltonians for two-dimensional (2D) higher-order topological phase with corner zero-energy states (CZESs). Our approach is based on the direct construction of an analytical solution of the CZESs in a series of 2D systems stacking the 1D extended Su-Schrieffer-Heeger (SSH) model, two copies of the two-band SSH model, along with two orthogonal directions. Fascinatingly, our approach not only gives the celebrated Benalcazar-Bernevig-Hughes and 2D SSH models but also reveals a novel model and we name it 2D crossed SSH model. Although these three models exhibit completely different bulk topology, we find that the CZESs can be universally characterized by edge winding number for 1D edge states, attributing to their unified Hamiltonian construction form and edge topology. Remarkably, our principle of constructing CZESs can be readily generalized to 3D and superconducting systems. Our work sheds new light on the theoretical understanding of the higher-order topological phases and paves the way to looking for higher-order topological insulators and superconductors.

DOI: 10.1103/PhysRevB.107.045118

I. INTRODUCTION

Over the past few years, the concept of topological phases has been generalized to higher order [1–4], which has been extensively studied in electronic [5–8], bosonic [9–15], Floquet [16–23], non-Hermitian [24–28], and quasicrystal systems [29–33]. Especially in condensed matter system, the higher-order topological insulators [34–38] and superconductors [39–45], featuring robust corner or hinge states, have been attracting increasing attention. Generally speaking, the corner states of higher-order topological phases with additional chiral or particle-hole symmetry, will appear at the center of their energy spectrum, namely zero energy. Particularly in the superconducting system with intrinsic particle-hole symmetry, the exact zero-energy corner states, dubbed as Majorana corner states, follow non-Abelian braiding statistics [46–48] and allow the implementation of topological quantum computation [49]. Recently, it has been shown that the corner zero-energy states (CZESs) in the electronic system also present nontrivial braiding properties [50].

The CZESs have been studied in various higher-order topological systems [51–63]. However, the established topological invariants characterization of CZESs is usually case by case. For example, the well-known Benalcazar-Bernevig-Hughes (BBH) [1,2] and 2D SSH models [64] are two paradigms featuring the CZESs, which are known to be characterized by quantized quadruple moment [65–67] and bulk polarization [64,68,69], respectively. Although exhibiting different topological characterizations, the BBH and 2D SSH models are both constructed from stacking the extended SSH models, two copies of the two-band SSH model [70]. This motivates us to systematically investigate the 2D systems consisting of stacking the 1D extended SSH models along different directions. For these systems, two open questions are urgent to be answered. First, do these systems always support the CZESs? Second, are there general topological characterizations for the obtained CZESs?

In this work, we establish a general analytical theory to provide the CZESs existing condition in the systems, stacking the 1D extended SSH model along two orthogonal directions. This condition not only naturally presents the BBH and 2D SSH models, but also leads to a novel model displaying second-order topology. As shown in Fig. 1(a), this model exhibits dimerized hoppings along both the x and y directions as the 1D SSH model but the dimerized hoppings along the y direction cross. We thus call it 2D crossed SSH model. We present a detailed study of the 2D crossed SSH model and find that the topology of the BBH, 2D SSH, and 2D crossed SSH models can be universally characterized by the well-defined edge winding number for 1D edge states, which elucidates the unified edge-corner correspondence [71–73]. Moreover, Our theory can be easily generalized to 3D and superconducting systems, and the mass of higher-order topological phases featuring the CZESs can be predicted.

II. CONSTRUCTING CORNER ZERO ENERGY STATES

Generally, we consider the 2D model Hamiltonian written as

$$H(\boldsymbol{k}) = \sum_{s=x,y} h_s(k_s),$$
$$h_s(k_s) = M_s(k_s)\Gamma_s^a + \lambda_s \sin k_s \Gamma_s^b, \tag{1}$$

*phyliuxin@hust.edu.cn

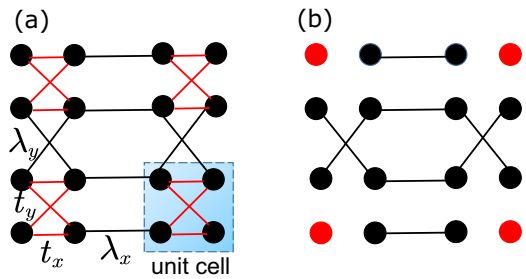

FIG. 1. Schematic diagram for the lattice hoppings of 2D crossed SSH model. (a) Red and black bonds represent the intracellular hoppings $t_{x,y}$ and intercellular hoppings $\lambda_{x,y}$, respectively. (b) The limit case $t_{x,y} = 0$ in (a).

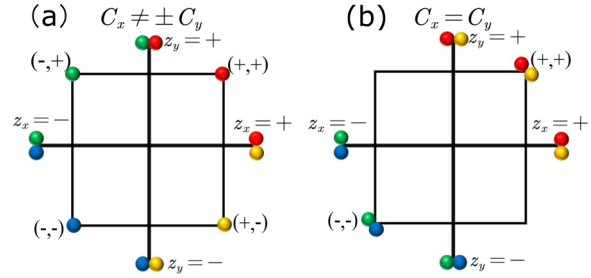

FIG. 2. (a, b) Schematic diagram of the end zero states and CZESs spatial distributions under different situations. The black square frame denotes the boundary of the 2D system described by the Hamiltonian H. The horizontal and perpendicular lines correspond to the 1D systems described by Hamiltonians h_x and h_y, respectively. The four color balls are the four common eigenstates of operators C_x and C_y, denoting the end zero states labeled by $z_{x/y}$ or CZESs, labeled by eigenvalues (z_x, z_y). The relation between the end zero states and CZESs can be guided by the color of the balls, which shows that the formation of the CZESs by the end zero states requires that the end zero states of different directions have the same spinor wave function part.

where $M_s(k_s)$ is $t_s + \lambda_s \cos k_s$ and $\Gamma_s^{a(b)}$, belonging to 15 traceless 4×4 Dirac matrices (see Appendix A), satisfy the anticommutation relation $\{\Gamma_s^a, \Gamma_s^b\} = 0$. Therefore, 1D Hamiltonian h_s respects chiral symmetry $C_s = i\Gamma_s^a\Gamma_s^b$, with $C_s^2 = 1$. As each Dirac matrix has twofold degenerate eigenvalues, the three Dirac matrices $\{\Gamma_s^a, \Gamma_s^b, C_s\}$ form the reducible representation of SU(2) Lie algebra: $h_s(k_s)$ can be considered as the direct sum of two copies of SSH models. Correspondingly, the topology of h_s is determined by the winding number ν_s of the vector $(M_s, \lambda_s \sin k_s)$ around the origin point. The topologically nontrivial phase is constrained in the region $|t_{x,y}| < |\lambda_{x,y}|$, corresponding to $\nu_s = 1$. Taking $s = x$ for example, each end exists two end zero states in the topologically nontrivial region, and their wave functions can be obtained by solving the equation

$$h_x(x)|\Psi_\alpha(x)\rangle = 0, \tag{2}$$

with $h_x(x)$ the real space Hamiltonian. We find that the end zero states are the eigenstates of C_x with eigenvalue $z_x = \pm 1$, and the end states labeled by $z_x = -1$ and $z_x = 1$ are localized at the left and right ends, respectively. Therefore, the 1D end zero states wave function can be generically written as

$$\left|\Psi_{z_x}^x(x)\right\rangle = f_{z_x}^x(x)\left|\psi_{z_x}^x\right\rangle, \tag{3}$$

where $f_{-(+)}^x(x)$ is the spatial wave function localized at the left (right) end and its analytical form is presented in Appendix B, the spinor $|\psi_{z_x}\rangle$ satisfies $C_x|\psi_{z_x}\rangle = z_x|\psi_{z_x}\rangle$.

Similarly, for the 1D Hamiltonian h_y, we have

$$h_y(y)\left|\Psi_{z_y}^y(y)\right\rangle = 0,$$
$$\left|\Psi_{z_y}^y(y)\right\rangle = f_{z_y}^y(y)\left|\psi_{z_y}^y(y)\right\rangle. \tag{4}$$

To understand the above solution visually, the end zero states labeled by the eigenvalue z_x or z_y are schematically denoted by the color balls in Figs. 2(a) and 2(b). However, we note that only the nontrivial topology of both h_x and h_y cannot guarantee the existence of CZESs for 2D Hamiltonian H. This can be best exemplified by the well-known Bernevig-Hughes-Zhang model [74], which satisfies the Hamiltonian form in Eq. (1) with $\Gamma_x^a = \Gamma_y^a$ and $\{\Gamma_x^b, \Gamma_y^b\} = 0$. Nevertheless, this case is known to host the gapless edge states rather than corner states. Remarkably, we find that the CZESs can be obtained when an additional general condition, namely $[C_x, C_y] = 0$ is satisfied. Under this condition, 4×4 matrices C_x and C_y have four common eigenstates $|\psi_{(z_x,z_y)}\rangle$, labeled by their eigenvalues (z_x, z_y), with $(z_x, z_y) \in \{(+,+), (+,-), (-,+), (-,-)\}$. Then we can construct the 2D wave function

$$|\Psi_{(z_x,z_y)}(\boldsymbol{r})\rangle = f_{z_x}^x(x)f_{z_y}^y(y)|\psi_{(z_x,z_y)}\rangle. \tag{5}$$

It is easy to see that

$$h_x(x)|\Psi_{(z_x,z_y)}(\boldsymbol{r})\rangle = 0, h_y(y)|\Psi_{(z_x,z_y)}(\boldsymbol{r})\rangle = 0, \tag{6}$$

resulting in $H(\boldsymbol{r})|\Psi_{(z_x,z_y)}(\boldsymbol{r})\rangle = 0$. The state $|\Psi_{(z_x,z_y)}(\boldsymbol{r})\rangle$ exponentially decays along both the x and y directions, which indicates that it is a CZES for the 2D system. Thus, we can conclude that $H(\boldsymbol{r})$ hosts four CZESs when $\nu_{x,y} = 1$ and $[C_x, C_y] = 0$. Notably, we have not considered any crystal symmetry limitations for H, which indicates that the CZESs can be realized when only local chiral symmetry is involved. Therefore, the obtained phases with CZESs belong to extrinsic higher-order topological phases [6,75].

Explicitly, the condition $[C_x, C_y] = 0$ can be divided into two situations, namely (a) $C_x \neq \pm C_y$ and (b) $C_x = \pm C_y$. For situation (a), the four common eigenstates of C_x and C_y form a complete set of basis in four-dimensional spinor space and these four nondegenerate states are labeled by the eigenvalues $(z_x, z_y) = \{(+,+), (+,-), (-,+), (-,-)\}$. Therefore, the corresponding four CZESs, schematically distinguished by the red, yellow, green, and blue balls in Fig. 2(a), are localized at each corner according to Eq. (5). For situation (b), the four common eigenstates of C_x and C_y have twofold degeneracies with $z_x = \pm z_y$. For example, when $C_x = C_y$, the four common eigenstates of C_x and C_y are labeled by $(z_x, z_y) = \{(+,+), (+,+), (-,-), (-,-)\}$. As a result, the four corresponding CZESs are localized at the diagonal corners with each corner a pair of CZESs, as shown in Fig. 2(b). On the contrast, when $C_x = -C_y$ the four CZESs are labeled by $(z_x, z_y) = \{(+,-), (+,-), (-,+), (-,+)\}$ and localized at the off-diagonal corners. Notably, up to now, our analysis is general and the specific form of $H(\boldsymbol{k})$ has not been given. However, the topological property of $H(\boldsymbol{k})$ deeply depends on

the given form. In the following, we perform the classification of $H(\boldsymbol{k})$ under the condition $[C_x, C_y] = 0$.

As any two Dirac matrices either commute or anticommute to each other and the anticommutation relation between $\Gamma^a_{x/y}$ and $\Gamma^b_{x/y}$ has been assigned, the second-order topological phase described by $H(\boldsymbol{k})$ can be further classified by the commutation relations between $\Gamma^{a,b}_x$ and $\Gamma^{a,b}_y$ under the condition $[C_x, C_y] = 0$, or equivalently $[i\Gamma^a_x\Gamma^b_x, C_y] = 0$. This condition means that both matrices Γ^a_x and Γ^b_x either commute or anticommute with C_y, written as $[\Gamma^{a,b}_x, C_y] = 0$ or $\{\Gamma^{a,b}_x, C_y\} = 0$. The former case further implies that matrices Γ^a_x and Γ^b_x commute or anticommute with both matrices Γ^a_y and Γ^b_y. The latter case indicates that both matrices Γ^a_x and Γ^b_x commute with one of the two matrices $\{\Gamma^a_y, \Gamma^b_y\}$ and anticommute with the another one. Therefore, there are four topologically inequivalent cases with the commutation relations

$$\begin{aligned}
&\text{(i)}: \left\{\Gamma^a_x, \Gamma^{a,b}_y\right\} = 0, \left\{\Gamma^b_x, \Gamma^{a,b}_y\right\} = 0;\\
&\text{(ii)}: \left[\Gamma^a_x, \Gamma^{a,b}_y\right] = 0, \left[\Gamma^b_x, \Gamma^{a,b}_y\right] = 0;\\
&\text{(iii)}: \left[\Gamma^a_x, \Gamma^{a,b}_y\right] = 0, \left\{\Gamma^b_x, \Gamma^{a,b}_y\right\} = 0;\\
&\text{(iv)}: \left[\Gamma^a_x, \Gamma^a_y\right] = 0, \left\{\Gamma^a_x, \Gamma^b_y\right\} = 0,\\
&\qquad \left\{\Gamma^b_x, \Gamma^a_y\right\} = 0, \left[\Gamma^b_x, \Gamma^b_y\right] = 0.
\end{aligned} \tag{7}$$

To show the possible realization of the above four types of commutation relations, we consider the concrete representation of the Dirac matrices. We define the 15 traceless Dirac matrices as $\{\Gamma^\alpha, \Gamma^\beta\} = 2\delta_{\alpha\beta}$, with $\alpha, \beta = 1, 2, 3, 4, 5$, and the other ten Dirac matrices are expressed as $\Gamma^{\alpha\beta} = [\Gamma^\alpha, \Gamma^\beta]/2i$. For instance, we may choose $\Gamma^{1,2,3} = \tau_3\sigma_{1,2,3}$, $\Gamma^4 = \tau_1\sigma_0$, $\Gamma^5 = \tau_2\sigma_0$, with τ_i and σ_i two sets of Pauli matrices and σ_0 the identity matrix. Without loss of generality, we choose $\{\Gamma^a_x, \Gamma^b_x, C_x\} = \{\Gamma^1, \Gamma^2, \Gamma^{21}\}$. We can list all possible choices of $\{\Gamma^a_y, \Gamma^b_y, C_y\}$ as

$$\begin{aligned}
&\text{(i)}: \{\Gamma^\alpha, \Gamma^\beta, \Gamma^{\beta\alpha}\};\\
&\text{(ii)}: \{\Gamma^{\alpha\beta}, \Gamma^{\beta\gamma}, \Gamma^{\alpha\gamma}\};\\
&\text{(iii)}: \{\Gamma^{2\alpha}, \Gamma^{2\beta}, \Gamma^{\beta\alpha}\};\\
&\text{(iv)}: \{\Gamma^{2\alpha}, -\Gamma^{1\alpha}, \Gamma^{21}\}, \{\Gamma^1, \Gamma^2, \Gamma^{21}\},\\
&\qquad \{\Gamma^{2\alpha}, \Gamma^2, -\Gamma^\alpha\}, \{\Gamma^1, \Gamma^{1\alpha}, \Gamma^\alpha\};
\end{aligned} \tag{8}$$

with $\alpha \neq \beta \neq \gamma \in (3, 4, 5)$. Therefore, the situations $C_x \neq \pm C_y$ and $C_x = \pm C_y$ correspond to cases (i–iv) and (iv), respectively. However, it can be readily verified that $H(\boldsymbol{k})$ has bulk chiral symmetry $\mathcal{C}$ with $\{\mathcal{C}, H(\boldsymbol{k})\} = 0$ for all the cases. Concretely, $\mathcal{C} = C_xC_y$ and $\mathcal{C} = C_x$ for cases (i–ii) and cases (iii–iv), respectively. Since the CZESs are the common eigenstates of C_x and C_y, the CZESs are the eigenstate of $\mathcal{C}$, with eigenvalue $z = z_xz_y$ or $z = z_x$. With this property, the CZESs labeled by the same eigenvalue of operator $\mathcal{C}$ cannot be coupled by the perturbation h_p preserving the bulk chiral symmetry $\mathcal{C}$ with $\{h_p, \mathcal{C}\} = 0$, because

$$\langle\Psi_z|h_p|\Psi_z\rangle, = z\langle\Psi_z|(\mathcal{C}h_p + h_p\mathcal{C})/2|\Psi_z\rangle = 0, \tag{9}$$

with $|\Psi_z\rangle$ the eigenstate of $\mathcal{C}$ with eigenvalue z. Consequently, the CZESs are topologically protected by the bulk chiral symmetry $\mathcal{C}$. For a similar reason, it can be shown that the chiral symmetry C_x and C_y also protect the CZESs, which implies that only the perturbation h_p, breaking all three chiral symmetries $\{\mathcal{C}, C_x, C_y\}$ simultaneously, can remove the CZESs.

Notably, once the commutation relations between the Dirac matrices are given by Eq. (7), the topological property of $H(\boldsymbol{k})$ are fully determined. In the case (i), matrices $\{\Gamma^a_{x,y}, \Gamma^b_{x,y}\}$ anticommute with each other and this scenario can be best exemplified by the celebrated BBH model. In case (ii), h_x and h_y commute with each other, corresponding to the 2D SSH model [64]. In cases (i) and (ii), the CZESs can be completely characterized by the topological invariant $\nu = \nu_x\nu_y$, which takes the value 1 or 0 and the value 1 corresponds to the presence of the CZESs. In the BBH and 2D SSH models, topological invariants (ν_x, ν_y) are revealed by topological invariants nested Wilson loop $(p_x^{\nu_y}, p_y^{\nu_x})$ [1,2] and bulk polarization (P_x, P_y) [64,76], respectively. Remarkably, cases (iii) and (iv) predict two unprecedented models, and case (iii) corresponds to the 2D crossed SSH model, which exhibits rich bulk phases and provides a new paradigm of second-order topological insulators. In the case (iv), we have $[\Gamma^a_x\Gamma^a_y, H] = 0$. Thus, $H(\boldsymbol{k})$ is block-diagonal in the eigenbasis of operator $\Gamma^a_x\Gamma^a_y$ and each block brings us to a two-band model (see Appendix C). We find that the CZESs in this two-band model always coexist with the edge flat band, which brings difficulty in identifying and characterizing the predicted CZSESs. Following, we mainly focus on the 2D crossed SSH model.

III. 2D CROSSED SSH MODEL

Considering the concrete representation of the Dirac matrices, the Hamiltonian for case (iii) can be written as

$$\begin{aligned}
\mathcal{H}(\boldsymbol{k}) &= h_x(k_x) + h_y(k_y),\\
h_x(k_x) &= M_x(k_x)\tau_x\sigma_0 + \lambda_x \sin k_x\tau_y\sigma_0,\\
h_y(k_y) &= M_y(k_y)\tau_x\sigma_x + \lambda_y \sin k_y\tau_x\sigma_y.
\end{aligned} \tag{10}$$

The corresponding lattice hopping of $\mathcal{H}(\boldsymbol{k})$ is schematically shown in Fig. 1(a), which has the dimerized hoppings along both the x and y directions as the 1D SSH model. Distinguished from the BBH and 2D SSH models, the two sets of dimerized hoppings along the y direction cross rather than parallel with each other. Therefore, we call this model the 2D crossed SSH model, which is essentially different from the BBH and 2D SSH models owing to the different commutation relations in Eq. (7). Note that the choice of chiral symmetry C_x for h_x is not unique such as $C_x = \tau_z\sigma_x$ or $C_x = \tau_z\sigma_y$. We explicitly define C_x as the product of the two Dirac matrices in h_x and similar for h_y. Only for this choice, the end states at the same end have the same eigenvalue of C_x and therefore are protected by C_x. Under our definition $C_x = -\tau_z\sigma_0$ and $C_y = -\tau_0\sigma_z$, which satisfies $[C_x, C_y] = 0$. Thus, when $|t_{x,y}| < |\lambda_{x,y}|$, the 2D crossed SSH model hosts four CZESs localized at the four corners of the system, which is consistent with the limit case $t_{x,y} = 0$ in Fig. 1(b) that there are one isolated atom at each corner.

To study the bulk phase and band structures of $\mathcal{H}(\boldsymbol{k})$, we simplify $\mathcal{H}(\boldsymbol{k})$ as

$$\mathcal{H}(\boldsymbol{k}) = M_x(k_x)\tau_x\sigma_0 + \lambda_x \sin k_x\tau_y\sigma_0 + E_y\tau_x\sigma_\varphi, \tag{11}$$

with $\sigma_\varphi = \cos\varphi\sigma_x + \sin\varphi\sigma_y$, $\cos\varphi = M_y/E_y$, $E_y = \sqrt{M_y^2 + (\lambda_y \sin k_y)^2}$. In the eigenbasis of σ_φ ($\sigma_\varphi = \pm 1$), $\mathcal{H}(\boldsymbol{k})$ is block-diagonal and the two block Hamiltonians can be written as

$$h_\pm(\boldsymbol{k}) = (M_x \pm E_y)\tau_x + \lambda_x \sin k_x \tau_y, \tag{12}$$

with $\pm$ the eigenvalues of σ_φ. As a result, we can reveal the 2D bulk spectrum of $\mathcal{H}(\boldsymbol{k})$ in Eq. (11) through the spectrum of $h_\pm(\boldsymbol{k})$, which can be considered as the 1D SSH model along the k_x direction with k_y-dependent intracell hopping $t_x \pm E_y$. With k_y given, the topology of 1D SSH Hamiltonians $h_\pm(\boldsymbol{k})$ is characterized by the quantized Berry phases $\alpha_\pm(k_y)$ of occupied states. We classify the bulk states of Eq. (11) into three phases based on the first-order topological band theory: when $\alpha_+(k_y)$ and $\alpha_-(k_y)$ are both quantized to π over all the range of k_y, the SSH models in Eq. (12) are fully gapped so that the bulk energy spectrum of $\mathcal{H}(\boldsymbol{k})$ in Eq. (11) is also fully gapped. In this case, the 2D system can be viewed as the pile-up of 1D topologically nontrivial SSH model, which is the weak topological insulator with flat edge band (see Appendix D 1); when $\alpha_+(k_y)$ and $\alpha_-(k_y)$ are both quantized to 0 over all the range of k_y, the SSH models in Eq. (12) and the bulk energy spectrum of $\mathcal{H}(\boldsymbol{k})$ in Eq. (11) are also fully gapped and the system is a trivial insulator; when $\alpha_+(k_y)$ or $\alpha_-(k_y)$ has a transition with varying k_y, the SSH models in Eq. (12) and the bulk energy spectrum of $\mathcal{H}(\boldsymbol{k})$ in Eq. (11) close their gaps at certain k_y along high symmetry line $k_x = 0$ or π. As the chiral operator $C = \tau_z\sigma_0$ anticommutes with the mirror-x operator $\mathcal{M}_x = \tau_x\sigma_0$, the degenerate two states at the nodal point have opposite eigenvalues of mirror-x. The perturbations preserving the mirror symmetry can not remove the nodes. Thus, we obtain the chiral symmetry and mirror symmetry protected Weyl semimetal, which is characterized by the edge flat bands (see Appendix D 1).

Having clarified the bulk phase, we display the bulk phase diagram in Fig. 3(a) under the parameters $\lambda_y = 1$, $t_y = 0.3$, and $0 < t_x < \lambda_x$. In this CZESs existing parameters region, the bulk states are divided into trivial insulator, weak topological insulator, and Weyl semimetal, which have been defined before. Owing to the existence of the CZESs, the trivial insulator listed here belongs to the second-order topological insulator in the category of higher-order topology. The yellow lines in Fig. 3(a) denote the bulk phase transitions associated with the creation or annihilation of a pair of Weyl nodes at high symmetry points. In Fig. 3(b), we numerically plot the real-space distribution of the CZESs in the second-order topological insulator phase. Our phase diagram shows that although the bulk phase transition occurs by closing the bulk energy gap, the CZESs exist through the whole phase transition process. The absence of one-to-one correspondence between the CZESs and bulk phase implies that the CZESs are not protected by bulk topology associated with $\alpha_\pm(k_y)$. In the following, we show that the CZESs can be characterized by the edge winding number for 1D edge states which can also detect the topology of the BBH and 2D SSH models.

Under the open boundary conditions along the x and y directions, the energy spectrum of the 2D crossed SSH model in a wire geometry is shown in Figs. 3(c) and 3(d), respectively. We find that there are edge-localized states along the x direction, corresponding to the in-gap red energy bands in Fig. 3(d). Notably distinguished from the edge states of the topological insulator, the edge states here extend over the whole 1D Brillouin zone. Therefore, these edge states can be described by truly 1D lattice Hamiltonian, which is essential to define edge winding number for 1D edge states unambiguously. Directly, the wave function of the edge states can be obtained by solving the equation $\mathcal{H}(k_x, y)|\Phi(k_x, y)\rangle_\alpha = E(k_x)|\Phi(k_x, y)\rangle_\alpha$. Note that the zero energy states of h_y are the eigenstates of C_y and $[h_x, C_y] = 0$, state $|\Psi(k_x, y)\rangle_\alpha$ can be considered as the common eigenstates of C_y and h_x with the requirements

$$\begin{aligned} h_y|\Phi(k_x, y)\rangle_\alpha &= 0, \\ h_x|\Phi(k_x, y)\rangle_\alpha &= E(k_x)|\Phi(k_x, y)\rangle_\alpha. \end{aligned} \tag{13}$$

Therefore, the wave function of these edge states can be written as

$$\begin{aligned} |\Psi(k_x, y)\rangle_{z_y} &= f_{z_y}^y(y) P_{z_y}|\phi(k_x)\rangle, \\ h_x(k_x)|\phi(k_x)\rangle &= E_x(k_x)|\phi(k_x)\rangle, \end{aligned} \tag{14}$$

where $E_x(k_x) = \sqrt{M_x^2 + (\lambda_x \sin k_x)^2}$ and the edge projection operator is $P_{z_y} = (1 + z_y C_y)$ with $z_y = \pm 1$. Here, the edge states $|\Phi(k_x, y)\rangle_-$ and $|\Psi(k_x, y)\rangle_+$ are localized close to the opposite edges. The edge Hamiltonian of describing these edge states can be extracted by projecting h_x to the zero-energy subspace defined by P_{z_y}. Picking up the nonzero block

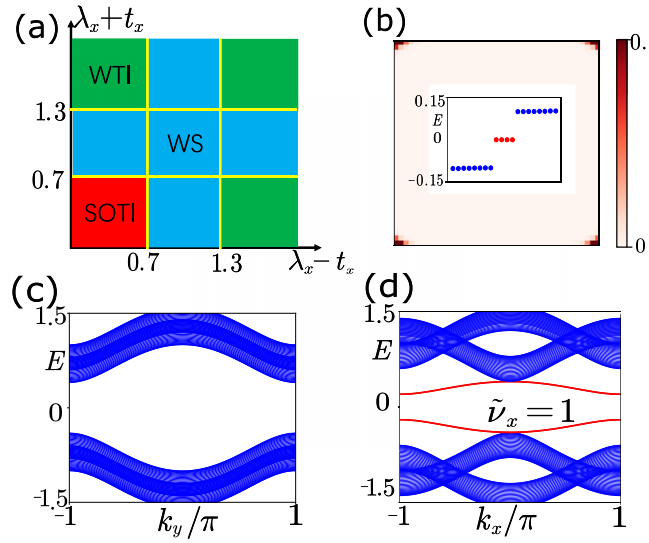

FIG. 3. (a) The phase diagram is plotted under the CZESs existing parameters region $t_y = 0.3$, $\lambda_y = 1$, $0 < t_x < \lambda_x$. The bulk phase transitions, represented by the yellow lines, divide the bulk states into weak topological insulator (WTI), Weyl semimetal (WS), and second-order topological insulator (SOTI) phases, corresponding to the green, blue, and red regions. (b) Spatial distribution of the CZESs in the 2D crossed SSH model, the inset plots the eigenenergies close to zero. (c) Energy dispersion of nanoribbon structure along the y direction. (d) Energy dispersion of nanoribbon structure along the x direction. The red bands denote the gapped edge states characterized by edge winding number $\tilde{\nu}_x = 1$. Common parameters in (b, c, d) are taken with $t_x = 0.1$, $\lambda_x = 0.2$, $t_y = 0.3$, $\lambda_y = 1$.

of P_{z_y}, the obtained edge Hamiltonian can be written as

$$\tilde{h}_x(k_x) = M_x(k_x)\tilde{\tau}_x + \lambda_x \sin k_x \tilde{\tau}_y, \tag{15}$$

with $\tilde{\tau}$ acting on the subspace defined by P_{z_y}. Obviously, $\tilde{h}_x(k_x)$ behaves as the SSH model and it is topologically nontrivial when $\nu_x = 1$. However, the existence of edge states depends on the condition that h_y is topologically nontrivial, namely $\nu_y = 1$. Thus, the edge winding number $\tilde{\nu}_x = 1$ defined by the occupied states of $\tilde{h}_x$ can precisely characterize the CZESs existing condition $\nu_{x,y} = 1$. Notably, the commutation relation $[h_x, C_y] = 0$ for the 2D crossed SSH model is the main reason for the existence of edge states and well-defined edge winding number $\tilde{\nu}_x$. Furthermore, it can be readily verified that $[h_x, C_y] = 0$ and $[h_y, C_x] = 0$ in cases (i) and (ii) according to the Eq. (7). Therefore, there are 1D edge states localized at the both x and y edges for the cases (i) and (ii), which is consistent with the previous numerical results of the edge energy spectrums in the BBH [1,2] and 2D SSH models [64]. Analogously, the edge Hamiltonians of these edge states in BBH and 2D SSH models behave as the 1D SSH model and the winding number defined by the edge states can characterize the CZESs. Moreover, the commutation relation $[h_x, C_y] = 0$ or $[h_y, C_x] = 0$ also leads to the CZESs existing condition $[C_x, C_y] = 0$, which further displays the correspondence between the 1D edge winding number and CZESs. Therefore, the edge winding number characterization method applies to the BBH, 2D SSH, and 2D crossed SSH models, which reveals the unified edge-corner correspondence [71–73].

IV. GENERALIZATION TO THREE-DIMENSIONAL AND SUPERCONDUCTING SYSTEMS

Our principle of constructing the CZESs can be easily generalized to a 3D cubic system. Here, we consider 3D eight-band Hamiltonian

$$\begin{aligned} H(\boldsymbol{k}) &= \sum_{s=x,y,z} h_s(k_s), \\ h_s(k) &= (t_s + \lambda_s \cos k_s)\Gamma^8_{as} + \lambda_s \sin k_s \Gamma^8_{bs}, \end{aligned} \tag{16}$$

where 8×8 Γ matrices Γ^8_{as} and Γ^8_{bs} (see Appendix A) anticommute with each other and the chiral symmetry of h_s is given by $C_s = i\Gamma^8_{as}\Gamma^8_{bs}$. Similarly, h_s can be deemed as the direct sum of four copies of SSH model and h_s has four end zero states at each end when $|t_s| < |\lambda_s|$. The end zero states of h_s are the eigenstates of C_s and the wave function of the end zero states can be generically written as

$$\left|\Psi^s_{z_s}(s)\right\rangle = f^s_{z_s}(s)\left|\psi^s_{z_s}\right\rangle, \tag{17}$$

where the spinor $|\psi^s_{z_s}\rangle$ is the eigenstate of C_s with the eigenvalue of $z_s = \pm 1$, and $f^s_{-,+}(s)$ is the scalar function localized close to the opposite ends.

Remarkably, when 8×8 matrices $\{C_x, C_y, C_z\}$ commute with each other, they have eight common eigenstates labeled as $|\psi_{z_x z_y z_z}\rangle$. Correspondingly, H hosts eight CZESs under the open boundary condition and the wave function of the CZESs can be written as

$$|\Psi_{z_x z_y z_z}(\boldsymbol{r})\rangle = \prod_{s=x,y,z} f^s_{z_s}(s)|\psi_{z_x,z_y,z_z}\rangle. \tag{18}$$

When $C_s \neq \pm C'_s$ for $\{s, s'\} \in \{x, y\}, \{x, z\}, \{y, z\}$, the eight common eigenstates of matrices $\{C_x, C_y, C_z\}$ form a complete set basis in eight-dimensional spinor space. In this case, every corner of the 3D cubic system described by H has one CZESs. Once the condition $C_s \neq \pm C'_s$ is relaxed, the eight common eigenstates must have the degeneracies owing to the limitation $z_s = \pm z'_s$, which gives rise to the multi CZESs localized at the certain corner of the 3D system. However, to determine the topological property of $H(\boldsymbol{k})$, we need to specify the commutation relations between all the Γ matrices in Eq. (16).

Our 2D classification indicates that there are four types of commutation relations between matrices $\{\Gamma^8_{as}, \Gamma^8_{bs}, \Gamma^8_{as'}, \Gamma^8_{bs'}\}$ under the condition $[C_s, C_{s'}] = 0$, with $\{s, s'\} \in \{x, y\}, \{x, z\}, \{y, z\}$. Thus, classifying $H(\boldsymbol{k})$ can predict 64 models featuring CZESs when are not distinguished the equivalent states between different directions. A typical example is the topological octupole insulator model [1,2,77], in which all the Γ matrices anticommute with each other. We will study other predicted models featuring the CZESs in our future work.

Notably, the topological property of our constructed theoretical model Hamiltonians does not depend on the chosen physics basis. If the constructed Hamiltonians are written in the superconducting Bogoliubov-de Gennes (BdG) basis, the obtained higher-order topological phase corresponds to the higher-order topological superconductors featuring Majorana corner states. For example, in the spinful Nambu basis $\Psi(\boldsymbol{k}) = (c_{\uparrow,\boldsymbol{k}}, c_{\downarrow,\boldsymbol{k}}, c^\dagger_{\uparrow,\boldsymbol{k}}, c^\dagger_{\downarrow,\boldsymbol{k}})$ with $c_{\uparrow,\boldsymbol{k}}$ the annihilate operator of the spin-up electron, we consider the superconducting BdG Hamiltonian

$$H_{\mathrm{BdG}} = \sum_{s=x,y} M_s(k_s)\Gamma^a_s + \lambda_s \sin k_s \Gamma^b_s. \tag{19}$$

The Hamiltonian H_{BdG} respects the particle-hole symmetry $\mathcal{P} = \rho_x K$ with the Pauli matrix ρ_x in the particle-hole space. Under the restriction of the particle-hole symmetry, we find that the commutation relations listed in Eq. (7) can be satisfied (see Appendix E) when considering the concrete representation of the Dirac matrices. Correspondingly, Hamiltonian H_{BdG} behaves as a second-order topological superconductor featuring Majorana corner states.

V. DISCUSSION AND CONCLUSION

Several studies show that the higher-order topological phases can be constructed by coupling a pair of lower-dimensional topological phases in a dimerized way [8,78–80]. Especially the 2D SSH models can be obtained through this construction method [81]. These studies usually only consider the nearest-neighbor hopping. Differently, our construction is based on the direct construction of the analytical solutions of the CZESs, which leads to the 2D crossed SSH model with the next-nearest-neighbor hopping.

Note that the 2D crossed SSH model shown in Fig. 1(a) has only the next-nearest-neighbor hopping along the y direction, and it is challenging to eliminate the coupling between

nearest neighbors. However, our further study (see Appendix F) shows that the CZESs are robust against a small nearest-neighbor hopping along the y direction, which reduces the experimental requirements for the realization of 2D crossed SSH model. Given the experimental realization of the BBH and 2D SSH models in various artificial lattice systems [10–12,82–86], we believe that the phononic crystals, acoustic crystals, and electrical circuits are promising platforms to realize the 2D crossed SSH model.

In summary, we establish a general theory of the higher-order topological phases emerging from SSH stacking. Our theory not only gives the well-known BBH and 2D SSH models but also predicts the 2D crossed SSH model. We establish the unified topological characterizing of these three models. Our work provides a broad venue for looking for higher-order topological phases.

ACKNOWLEDGMENTS

X.L. acknowledges the support from Innovation Program for Quantum Science and Technology (Grant No. 2021ZD0302700) and National Natural Science Foundation of China (NSFC) (Grant No. 12074133). C.-X.L. acknowledges the support through the Penn State MRSEC–Center for Nanoscale Science via NSF Award No. DMR-2011839.

APPENDIX A: DIRAC MATRICES AND THEIR GENERALIZATION

Starting from the three anticommuting Pauli matrices $\sigma_{x,y,z}$ and 2×2 identity matrix σ_0, the 16 Dirac matrices can be generated by their direct product, showing as $\Gamma^p_{ij}=\sigma_i\otimes\sigma_j(\sigma_i\sigma_j)$, with $i=j=x,y,z,0$ and matrix dimension index $p=4$. Besides 4×4 identify matrix, the other 15 Dirac matrices are traceless and square to identify. In the 15 traceless Dirac matrices, the five of them anticommute with each other. Without loss of generality, we choose the five anticommuting matrices as

$$\Gamma^4_1=\sigma_z\sigma_x,\ \Gamma^4_2=\sigma_z\sigma_y,$$
$$\Gamma^4_3=\sigma_z\sigma_z,\ \Gamma^4_4=\sigma_x\sigma_0,\ \Gamma^4_5=\sigma_y\sigma_0. \tag{A1}$$

These anticommuting matrices act as the generators and the other 10 traceless Dirac matrices can be generated by $\Gamma^4_{mn}=\frac{1}{2i}[\Gamma^4_m,\Gamma^4_n]$, with $m=n=1,2,3,4,5$.

Generalizing to higher dimension, the direct product of arbitrary d sets of Pauli matrices can generate 4^d Γ matrices $\Gamma^{2^d}_{i,\cdots,j\cdots,k}=\sigma_i\cdots\sigma_j\cdots\sigma_k$, with the matrix dimension $2^d\times 2^d$. In these 4^d Γ matrices, $2d+1$ matrices anticommute with each other, forming complex Clifford algebra. Generally, the $2d+1$ anticommuting matrices can be obtained through the iteration from $2d-1$ anticommuting Γ matrices

$$\Gamma^{2^d}_{1,2,\cdots,2d-1}=\sigma_z\otimes\Gamma^{2^{d-1}}_{1,2,\cdots,2d-1},\ \Gamma^{2^d}_{2d}=\sigma_x\otimes I^{2^{d-1}},$$
$$\Gamma^{2^d}_{2d+1}=\sigma_y\otimes I^{2^{d-1}}, \tag{A2}$$

where $I^{2^{d-1}}$ denotes the $2^{d-1}\times 2^{d-1}$ identify matrix, and $\Gamma^{2^{d-1}}_{1,2,\cdots,2d-1}$ represents $2d-1$ anticommuting Γ matrices with matrix dimension $2^{d-1}\times 2^{d-1}$. These anticommuting matrices act as generators and other Γ matrices can be generated by their successive products.

When $d=3$, there are seven Γ matrices anticommuting with each other, and we choose them as

$$\Gamma^8_{1,2,3,4,5}=\sigma_z\otimes\Gamma^4_{1,2,3,4,5},\ \Gamma^8_6=\sigma_x\sigma_0\sigma_0,\ \Gamma^8_7=\sigma_y\sigma_0\sigma_0. \tag{A3}$$

With these seven anticommuting Γ matrices, other 8×8 Γ matrices can be generated by the successive products of two or three anticommuting Γ matrices, showing as $i\Gamma_m\Gamma_n$ or $i\Gamma_m\Gamma_n\Gamma_l$, with $m,n,l=1,\cdots,7$.

APPENDIX B: 1D EXTENDED SSH MODEL

In the momentum space, we consider the 1D model Hamiltonian

$$h(k)=M(k)\Gamma^p_1+\lambda\sin k\Gamma^p_2, \tag{B1}$$

where $M(k)=(t+\lambda\cos k)$, $\Gamma^p_{1,2}$ are $p\times p$ Γ matrices and satisfy the anticommutation relation $\{\Gamma^p_1,\Gamma^p_2\}=0$. For our purpose, we following consider the two cases $p=4$ and 8. When $p=4$, we know that there are three additional Γ matrices $\Gamma^4_{3,4,5}$ anticommuting with $\Gamma^4_{1,2}$. Thus, we have the commutation relation $[i\Gamma^4_3\Gamma^4_4,h(k)]=0$, which implies that 1D Hamiltonian $h(k)$ is block-diagonal in the eigenbasis of matrix $i\Gamma^4_3\Gamma^4_4$. In this case, each 2×2 block Hamiltonian behaves as the two-band SSH model. Thus, $h(k)$ is the direct sum of two SSH models. When $p=8$, we know that there are five additional Γ matrices anticommuting with the matrices $\Gamma^8_{1,2}$. Thus, we have the commuting relations $[i\Gamma^8_3\Gamma^8_4,h(k)]=0$ and $[i\Gamma^8_5\Gamma^8_6,h(k)]=0$, which imply that $h(k)$ is block-diagonal in the common eigenbasis of matrices $i\Gamma^8_3\Gamma^8_4$ and $i\Gamma^8_5\Gamma^8_6$. In this case, $h(k)$ is made of the direct sum of four blocks and each block behaves as the two-band SSH model. Because $h(k)$ always can be viewed as the direct sum of multiple copies of the SSH model, we call it the extended SSH model.

In Eq. (B1), the chiral symmetry of h can be written as $C=i\Gamma^p_1\Gamma^p_2$, with $\{C,h\}=0$. Thus, 1D Hamiltonian h belongs to the AIII symmetry class with Z topological classification. We now calculate the topological invariant winding number to characterize the band topology of $h(k)$. The energy spectrum of h is $E=\sqrt{(t+\lambda\cos k)^2+(\lambda\sin k)^2}$. For simplicity, h can be normalized as

$$\bar{h}=\cos\varphi\Gamma^p_1+\sin\varphi\Gamma^p_2, \tag{B2}$$

with $\cos\varphi=(t+\lambda\cos k)/E$. Then the winding number contributed by the occupied states can be calculated as [87]

$$\begin{aligned}\nu&=-\frac{1}{4i\pi}\int_{-\pi}^{\pi}\mathrm{Tr}[C\bar{h}d\bar{h}]\\&=-\frac{1}{4i\pi}\int_{-\pi}^{\pi}\mathrm{Tr}\big[(\cos\varphi\partial_k\cos\varphi+\sin\varphi\partial_k\sin\varphi)C\\&\quad+(\cos\varphi\partial_k\sin\varphi-\sin\varphi\partial_k\cos\varphi)C\Gamma^p_1\Gamma^p_2\big]\\&=\frac{p}{4\pi}\int_{-\pi}^{\pi}(\cos\varphi\partial_k\sin\varphi-\sin\varphi\partial_k\cos\varphi)\\&=\frac{p}{4\pi}\int_{-\pi}^{\pi}\partial_k\varphi.\end{aligned} \tag{B3}$$

Here, we have used the traceless property of matrix C. In the parameter region $|t| < |\lambda|$, the above integration yields topological invariant $\nu = p/2$; otherwise, $\nu = 0$. Owing to the bulk-boundary correspondence, the nonzero winding number ν means that there are $p/2$ end zero states localized at each end under the open boundary condition. In the following, we solve the analytical wave function of these end zero states.

Considering the semi-infinite system ($r > 0$) described by h, we solve the end zero states localized close to the end $r = 0$. Expanding $h(k)$ at $k = 0$ to second order of k and replacing $k \to -i\partial_r$, we have

$$h(-i\partial_r) = \left(m + \lambda/2\partial_r^2\right)\Gamma_1^p - i\lambda\partial_r\Gamma_2^p, \tag{B4}$$

with $m = t + \lambda$. Solving the eigen equation $h(-i\partial_r)|\Phi_\alpha(r)\rangle = 0$ gives rise to

$$\left(m + \lambda/2\partial_r^2\right)\Gamma_1^p|\Phi_\alpha(r)\rangle - i\lambda\partial_r\Gamma_2^p|\Phi_\alpha(r)\rangle = 0. \tag{B5}$$

Multiplying both sides by Γ_1^p gives

$$\left(m + \lambda/2\partial_r^2\right)|\Phi_\alpha(r)\rangle = \lambda\partial_r C|\Phi_\alpha(r)\rangle. \tag{B6}$$

Therefore, state $|\Phi_\alpha(r)\rangle$ should be the eigenstate of chiral operator C, namely $C|\Phi_z(r)\rangle = z|\Phi_z(r)\rangle$ with $z = \pm 1$. We set the trial wave function $|\Phi_z(r)\rangle = e^{\xi_z r}|\psi_z\rangle$, where $C|\psi_z\rangle = z|\psi_z\rangle$ and ξ_z is a complex number. By inserting this ansatz solution into Eq. (B6), we have

$$\lambda/2\xi_z^2 - z\lambda\xi + m = 0. \tag{B7}$$

The two roots are $\xi_z^{1,2} = \frac{z\lambda \pm \sqrt{\lambda^2 - 2m\lambda}}{\lambda}$. In the region $|t| < |\lambda|$, the real part of $\xi_z^{1,2}$ are negative and positive when $z = -1$ and $z = 1$, respectively. Under the boundary condition $|\Phi_z(0)\rangle = |\Phi_z(\infty)\rangle = 0$ restrictions, the wave function of end states can be written as

$$|\Phi_-(r)\rangle = \mathcal{N}(e^{\xi_-^1 r} - e^{\xi_-^2 r})|\psi_-\rangle, \tag{B8}$$

with the normalization factor $\mathcal{N}$.

In the contrast, if we consider the semi-infinite system $r < 0$, then we will find that the end zero states should be the eigenstate of the chiral operator C with eigenvalue $z = 1$. As a result, for a finite system with length L, the end zero states localized close to the end $r = 0$ and $r = L$ are the eigenstates of the chiral operator C, with eigenvalue $z = -1$ and $z = 1$, respectively. For $p \times p$ matrix C, there are $p/2$ eigenstates with eigenvalue $z = 1$ and $z = -1$, respectively. Thus, there are $p/2$ end zero states localized at each end for $h(r)$. In the main text, we take $p = 4$ and $p = 8$, then there are two and four end zero states localized at each end, respectively. The spatial parts of the wave function for these end zero states are

$$\begin{aligned} f_-^s(r_s) &= \mathcal{N}_s^-(e^{\xi_-^1 r_s} - e^{\xi_-^2 r_s}), \\ f_+^s(r_s) &= \mathcal{N}_s^+(e^{\xi_+^1 (r_s - L_s)} - e^{\xi_+^2 (r_s - L_s)}), \end{aligned} \tag{B9}$$

where $\mathcal{N}_s^-, \mathcal{N}_s^+$ are the normalization factors, and the index s denotes the different directions.

APPENDIX C: THE MODEL PREDICTED BY THE COMMUTATION RELATION (IV)

Considering the concrete representations of the Γ matrices, the bulk Hamiltonian, corresponding to the commutation relation (iv) in Eq. (7), can be written as

$$\begin{aligned} \mathcal{H}^{\rm iv}(\boldsymbol{k}) &= h_x^{\rm iv}(k_x) + h_y^{\rm iv}(k_y), \\ h_x^{\rm iv}(k_x) &= M_x(k_x)\tau_z\sigma_x + \lambda_x \sin k_x \tau_z\sigma_y, \\ h_y^{\rm iv}(k_y) &= M_y(k_y)\tau_0\sigma_x + \lambda_y \sin k_y \tau_0\sigma_y, \end{aligned} \tag{C1}$$

with τ, σ two sets Pauli matrices. The lattice hopping of $\mathcal{H}^{\rm iv}(\boldsymbol{k})$ is shown in Figs. 4(d) and 4(h). For this concrete model, we have chiral symmetries $C_x^{\rm iv} = C_y^{\rm iv} = -\sigma_z$ which commute with each other. $\mathcal{H}^{\rm iv}$ is block diagonal in τ space and the two block Hamiltonians can be written as $h_\pm^{\rm iv} = (\pm M_x + M_y)\sigma_x + (\pm\lambda_x \sin k_x + \lambda_y \sin k_y)\sigma_y$. Here, h_+ and h_- have the identical physics and we focus on the Hamiltonian $h_+^{\rm iv}$. This two-band model can be separated into two 1D Hamiltonians as $h_+ = h_x' + h_y'$, with $h_s' = (t_s' + \lambda_s \cos k_s)\sigma_x + \lambda_s \sin k_s \sigma_y$ and $t_x' + t_y' = t_x + t_y = t$. As long as h_x' and h_y' are topologically nontrivial with end zero states, the 2D Hamiltonian h_+ has CZESs localized at the diagonal corners. Thus, there are CZESs for h_+ when $|t| < |\lambda_x| + |\lambda_y|$.

$h_+^{\rm iv}$ can be viewed as a modulated SSH along $k_{x/y}$, with $k_{y/x}$ given. The band structures can be clearly revealed by the Berry phase $\nu^{\rm iv}(k_x)$ or $\nu^{\rm iv}(k_y)$ of the occupied state of h_+, with k_x or k_y given. When $\nu^{\rm iv}(k_x)$ or $\nu^{\rm iv}(k_y)$ is quantized to π over all the range, the bulk states behave as a weak topological insulator characterized by edge flat band, corresponding to the condition $|t| + |\lambda_x| < |\lambda_y|$ or $|t| + |\lambda_y| < |\lambda_x|$. When $\nu^{\rm iv}(k_y)$ and $\nu^{\rm iv}(k_x)$ are both quantized to 0 over all the range, corresponding to the condition $|t| > |\lambda_x| + |\lambda_y|$, the bulk is a normal insulator. When $\nu^{\rm iv}(k_x)$ or $\nu^{\rm iv}(k_y)$ is not successive, corresponding to the condition $||t| - |\lambda_x|| < |\lambda_y| < |t| + |\lambda_x|$ or $||t| - |\lambda_y|| < |\lambda_x| < |t| + |\lambda_y|$, the bulk is a Weyl semimetal characterized by edge flat band. Therefore, distinguished from case (iii), the predicted CZESs here always coexist with the edge flat band, which brings difficulty to identify and characterize the predicted CZESs.

APPENDIX D: THE BBH, 2D SSH, AND 2D CROSSED SSH MODELS

1. Band structures

Considering the concrete matrix representations of commutation relations (i–iii) in Eq. (7), we obtain the model Hamiltonians

$$\begin{aligned} \mathcal{H}^{\rm g}(\boldsymbol{k}) &= h_x^{\rm g}(k_x) + h_y^{\rm g}(k_y), \\ h_x^{\rm i,ii,iii} &= M_x(k_x)\tau_x\sigma_0 + \lambda_x \sin k_x \tau_y\sigma_0, \\ h_y^{\rm i} &= M_y(k_y)\tau_z\sigma_x + \lambda_y \sin k_y \tau_z\sigma_y, \\ h_y^{\rm ii} &= M_y(k_y)\tau_0\sigma_x + \lambda_y \sin k_y \tau_0\sigma_y, \\ h_y^{\rm iii} &= M_y(k_y)\tau_x\sigma_x + \lambda_y \sin k_y \tau_x\sigma_y, \end{aligned} \tag{D1}$$

with index g = i,ii,iii, corresponding to different cases. The Hamiltonians $\mathcal{H}^{\rm i}(\boldsymbol{k})$, $\mathcal{H}^{\rm ii}(\boldsymbol{k})$, and $\mathcal{H}^{\rm iii}(\boldsymbol{k})$ describe the BBH, 2D SSH, and 2D crossed SSH model, respectively. For

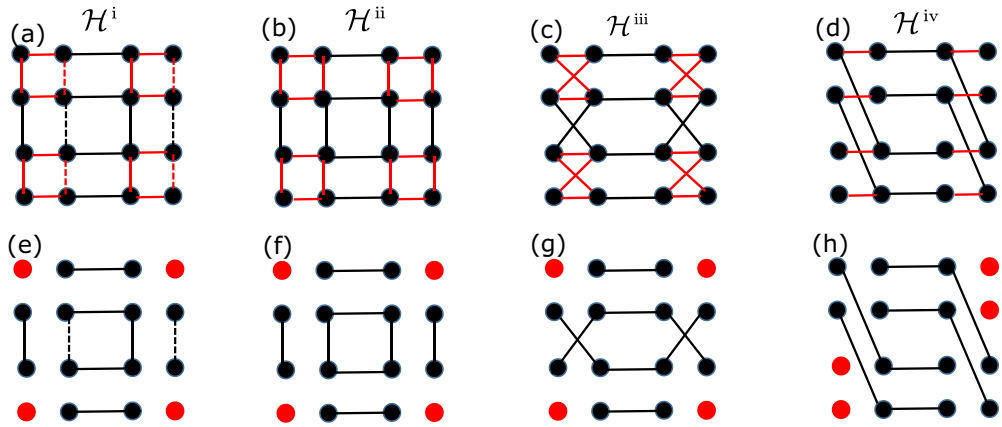

FIG. 4. (a–d) The schematic diagram of the lattice hoppings for Hamiltonians $\mathcal{H}^{\text{i-iv}}$. The red and black bonds represent the intracellular and intercellular hoppings, respectively. (e–h) Schematic of the lattice hoppings in the limit case $t_x = t_y = 0$ for Hamiltonians $\mathcal{H}^{\text{i-iv}}$. The presence of the isolated atoms at the corners in this limit case corresponds to the CZESs. For (e–g), the existence of isolated edge atoms coupled in a dimerized way corresponds to the existence of edge states described by the SSH model.

Hamiltonians $\mathcal{H}^{\text{i,ii,iii}}(\boldsymbol{k})$, we have the chiral symmetries

$$\begin{aligned} C_x^{\mathrm{i}} &= -\tau_z\sigma_0, C_y^{\mathrm{i}} = -\tau_0\sigma_z, \left[C_x^{\mathrm{i}}, C_y^{\mathrm{i}}\right] = 0, \\ C_x^{\mathrm{ii}} &= -\tau_z\sigma_0, C_y^{\mathrm{ii}} = -\tau_0\sigma_z, \left[C_x^{\mathrm{ii}}, C_y^{\mathrm{ii}}\right] = 0, \\ C_x^{\mathrm{iii}} &= -\tau_z\sigma_0, C_y^{\mathrm{iii}} = -\tau_0\sigma_z, \left[C_x^{\mathrm{iii}}, C_y^{\mathrm{iii}}\right] = 0, \end{aligned} \tag{D2}$$

where $\{C_s^{\mathrm{g}}, h_s^{\mathrm{g}}\} = 0$, with indexes $s = x, y$. The three models $\mathcal{H}^{\text{i,ii,iii}}$ respect the bulk chiral symmetry

$$\begin{aligned} \mathcal{C}^{\mathrm{i}} &= C_x^{\mathrm{i}} C_y^{\mathrm{i}} = \tau_z\sigma_z, \ \mathcal{C}^{\mathrm{ii}} = C_x^{\mathrm{ii}} C_y^{\mathrm{ii}} = \tau_z\sigma_z, \\ \mathcal{C}^{\mathrm{iii}} &= C_x^{\mathrm{iii}} = -\tau_z\sigma_0, \end{aligned} \tag{D3}$$

with $\{\mathcal{C}^{\mathrm{g}}, \mathcal{H}^{\mathrm{g}}\} = 0$. The lattice hoppings, corresponding to Hamiltonians $\mathcal{H}^{\text{i,ii,iii}}(\boldsymbol{k})$, are schematically shown in Figs. 4(a)–(c). In Figs. 4(e)–(g), the presence of isolated atoms at the corners in the limit case $t_{x,y} = 0$ corresponds to the existence of the CZESs.

To reveal the band structures of the Hamiltonians $\mathcal{H}^{\text{i,ii,iii}}(\boldsymbol{k})$, we rewrite these Hamiltonians as

$$\begin{aligned} \mathcal{H}^{\mathrm{i}}(\boldsymbol{k}) &= M_x(k_x)\tau_x\sigma_0 + \lambda_x \sin k_x \tau_y\sigma_0 + E_y\tau_z\sigma_\varphi, \\ \mathcal{H}^{\mathrm{ii}}(\boldsymbol{k}) &= M_x(k_x)\tau_x\sigma_0 + \lambda_x \sin k_x \tau_y\sigma_0 + E_y\tau_0\sigma_\varphi, \\ \mathcal{H}^{\mathrm{iii}}(\boldsymbol{k}) &= M_x(k_x)\tau_x\sigma_0 + \lambda_x \sin k_x \tau_y\sigma_0 + E_y\tau_x\sigma_\varphi, \end{aligned} \tag{D4}$$

where we have defined $E_y = \sqrt{M_y^2 + (\lambda_y \sin k_y)^2}$ and $\sigma_\varphi = \cos\varphi\sigma_x + \sin\varphi\sigma_y$, with $\tan\varphi = \lambda_y \sin k_y / M_y$. Thus, in the eigenbasis of σ_φ, $\mathcal{H}^{\text{i,ii,iii}}$ are block-diagonal and two blocks Hamiltonians are

$$\begin{aligned} h_\pm^{\mathrm{i}}(\boldsymbol{k}) &= M_x(k_x)\tau_x + \lambda_x \sin k_x \tau_y \pm E_y\tau_z, \\ h_\pm^{\mathrm{ii}}(\boldsymbol{k}) &= M_x(k_x)\tau_x + \lambda_x \sin k_x \tau_y \pm E_y\tau_0, \\ h_\pm^{\mathrm{iii}}(\boldsymbol{k}) &= (M_x(k_x) \pm E_y)\tau_x + \lambda_x \sin k_x \tau_y, \end{aligned} \tag{D5}$$

with $\pm$ the eigenvalues of σ_φ. With given a k_y, $h_\pm^{\mathrm{i}}$, $h_\pm^{\mathrm{ii}}(\boldsymbol{k})$, and $h_\pm^{\mathrm{iii}}(\boldsymbol{k})$ can be viewed as the SSH model along k_x, with additional chiral symmetry breaking term $\pm E_y\tau_z$, modulated chemical potential term $\pm E_y\tau_0$, modulated intracell hopping term $\pm E_y\tau_x$, respectively. According to the Eq. (D5), we know that the bulk energy spectrums of Hamiltonians $\mathcal{H}^{\text{i-iii}}(\boldsymbol{k})$ can be written as

$$\begin{aligned} E^{\mathrm{i}}(\boldsymbol{k}) &= \pm\sqrt{E_x^2 + E_y^2}, \quad E^{\mathrm{ii}}(\boldsymbol{k}) = \pm E_x \pm E_y, \\ E^{\mathrm{iii}}(\boldsymbol{k}) &= \pm\sqrt{(M_x \pm E_y)^2 + (\lambda_x \sin k_x)^2}, \end{aligned} \tag{D6}$$

with $E_x = \sqrt{M_x^2 + (\lambda_x \sin k_x)^2}$. Thus, for $\mathcal{H}^{\mathrm{i}}(\boldsymbol{k})$, as long as $E_x \neq 0$ and $E_y \neq 0$, the bulk states are fully gapped. For $\mathcal{H}^{\mathrm{ii}}(\boldsymbol{k})$, when $|E_x|_{\min} < |E_y|_{\max}$ or $|E_y|_{\min} < |E_x|_{\max}$, the bulk states are fully gapped. Otherwise, the bulk states are gapless and behave as a metal. For $\mathcal{H}^{\mathrm{iii}}(\boldsymbol{k})$, when $||t_x| - |E_y||_{\min} > |\lambda_x|$, the bulk states are fully gapped and behave as a trivial insulator or a second-order topological insulator when $|t_{x,y}| < |\lambda_{x,y}|$. When $|t_x| + |E_y|_{\max} < |\lambda_x|$, or $||t_x| - |E_y||_{\max} < |\lambda_x|$ and $|t_x| + |E_y|_{\min} > |\lambda_x|$, the bulk states are fully gapped and behave as a weak topological insulator characterized by the edge flat bands, as shown in Figs. 5(a) and 5(b). Otherwise, the bulk states are gapless and behave as mirror symmetry-protected Weyl semimetal characterized by edge flat bands, as shown in Figs. 5(c)–(f).

When the bulk states are fully gapped, the wave function of the occupied states for Hamiltonians $\mathcal{H}^{\text{i-iii}}(\boldsymbol{k})$ can be written as

$$\begin{aligned} \left|\Psi_1^{\mathrm{i}}\right\rangle &= (\sin\theta/2, -\cos\theta/2e^{i\phi})^T \otimes (1, e^{i\varphi})^T/\sqrt{2}, \\ \left|\Psi_2^{\mathrm{i}}\right\rangle &= (\cos\theta/2, -\sin\theta/2e^{i\phi})^T \otimes (1, -e^{i\varphi})^T/\sqrt{2}, \\ \left|\Psi_1^{\mathrm{ii}}\right\rangle &= (1, e^{i\phi})^T \otimes (1, -e^{i\varphi})^T/2, \\ \left|\Psi_2^{\mathrm{ii}}\right\rangle &= (1, -e^{i\phi})^{\mathrm{T}} \otimes (1, -e^{i\varphi})^T/2, \\ \left|\Psi_1^{\mathrm{iii}}\right\rangle &= (1, -e^{i\beta_1})^T \otimes (1, e^{i\varphi})^T/2, \\ \left|\Psi_2^{\mathrm{iii}}\right\rangle &= (1, -e^{i\beta_2})^T \otimes (1, -e^{i\varphi})^T/2, \end{aligned} \tag{D7}$$

with $\cos\theta = E_y/|E^{\mathrm{i}}|$, $\tan\phi = \lambda_x \sin k_x/M_x$, $\tan\beta_1 = \lambda_x \sin k_x/(M_x + E_y)$, and $\tan\beta_2 = \lambda_x \sin k_x/(M_x - E_y)$. Here,

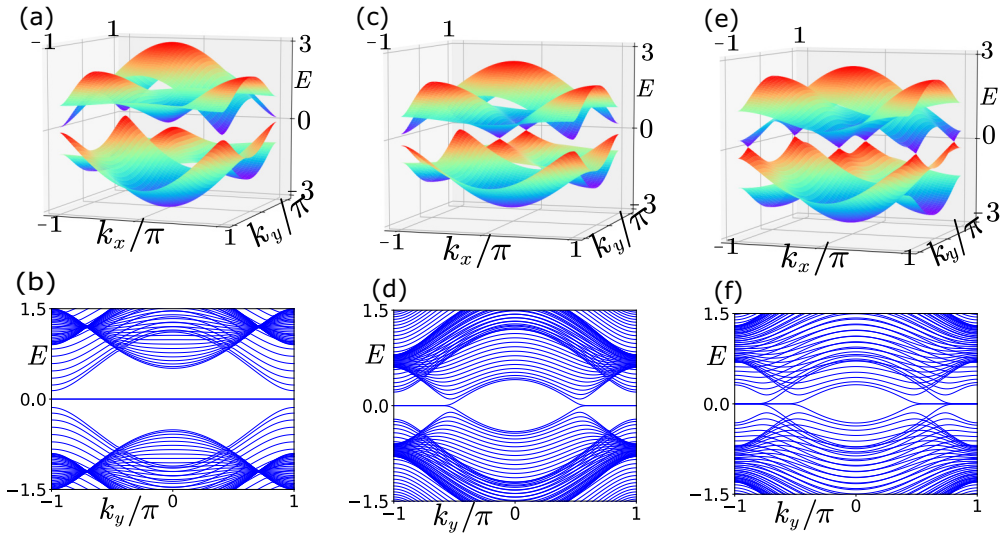

FIG. 5. (a, b) The bulk energy spectrums and edge flat bands of the weak topological insulator phase are plotted. We take the parameters as $\lambda_x = 1$, $t_x = 0.6$, $\lambda_y = 1$, $t_y = 0.5$. (c, d) The bulk energy spectrums and edge flat bands of the Weyl semimetal with two Weyl points are plotted. We take the parameters as $\lambda_x = 1, t_x = 0.6, \lambda_y = 0.7, t_y = 0.4$. (e, f) The bulk energy spectrums and edge flat bands of the Weyl semimetal with four Weyl points are plotted. We take the parameters as $\lambda_x = 1$, $t_x = 0.6$, $\lambda_y = 1$, $t_y = 0.2$.

the state $|\Psi_n^g\rangle$ denotes the nth occupied state of $\mathcal{H}^{\rm g}(\boldsymbol{k})$, with $n = 1, 2$.

2. Topological characterizations

For characterizing the CZESs, several topological invariants have been established, including nested Wilson loop $(p_x^{\nu_y}, p_y^{\nu_x})$ [1,2], edge polarization [1,2], and bulk polarization (P_x, P_y) [64,68,69,76]. Here, we test the applicability of characterizing the 2D crossed SSH model by these topological invariants and compare them to the characterization of the BBH and 2D SSH models.

The nested Wilson loop characterization for the CZESs is based on the gapped Wannier bands [1,2]. For the BBH model, the Wannier bands are gapped and the nested Wilson loop method can characterize the CZESs [1,2]. For the 2D SSH and 2D crossed SSH models, the Wannier bands are gapless, as shown in Figs. 6(a) and 6(b), respectively. Therefore, the nested Wilson loop characterization method only applies to the BBH model.

For the 2D SSH model, it is shown that the CZESs can be characterized by the bulk polarization [64,68,69]. The polarization of nth occupied state along the x direction can be written as

$$P_n^{\rm g} = \frac{1}{4\pi^2}\int dk_y \nu_n^{\rm g}(k_y),$$
$$\nu_n^{\rm g}(k_y) = i\int dk_x \langle \Psi_n^{\rm g}(\boldsymbol{k})|\partial_{k_x}|\Psi_n^{\rm g}(\boldsymbol{k})\rangle, \tag{D8}$$

where $\nu_n^{\rm g}(k_y)$ is the Berry phase for occupied state $|\Psi_n^{\rm g}\rangle$. For the 2D SSH model, $\nu_1^{\rm ii}$ and $\nu_2^{\rm ii}$ are both quantized to π (0), corresponding to the existence (absence) of CZESs, and therefore $P_n^{\rm ii}$ can characterize the 2D SSH model. For the BBH model, $\nu_1^{\rm i}$ and $\nu_2^{\rm i}$ are not quantized and they can take the same values no matter CZESs exist or not. Therefore the CZESs cannot be characterized by bulk polarization. For the 2D crossed SSH model, Berry phases $\nu_1^{\rm iii}$ and $\nu_2^{\rm iii}$ take value 0 for the SOTI phase in Fig. 3(a), and therefore bulk polarization cannot characterize the CZESs.

The BBH model can be characterized by the quantized edge polarizations $p_x^{\rm edge} = p_y^{\rm edge} = 0.5$. For the 2D crossed SSH model, there are edge states only along the x direction. Correspondingly, the 2D crossed SSH model exhibits nontrivial edge polarization only along the x direction, as shown in Figs. 7(a) and 7(b). For completeness, we also calculate the quantized corner charge of the 2D crossed SSH model, as shown in Fig. 7(c).

In the main text, we have shown that the edge winding number $\tilde{\nu}_x = 1$ can completely reflect the CZESs existing condition $\nu_{x,y} = 1$. For the BBH and 2D SSH models, there are edge states along the k_x and k_y directions, as shown in Figs. 8(a) and 8(b) and Figs. 8(c) and 8(d), respectively. Generally, the wave function of the edge states along k_x and k_y can be written as

$$|\Psi^{\rm g}(k_x, y)\rangle_{z_y} = f_{z_y}^{\rm g}(y) P_{z_y}^{\rm g}|\psi^{\rm g}(k_x)\rangle,$$
$$h_x^{\rm g}(k_x)|\psi^{\rm g}(k_x)\rangle = E_x(k_x)|\psi^{\rm g}(k_x)\rangle,$$

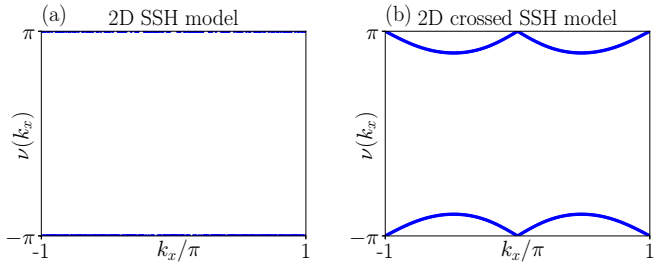

FIG. 6. (a) The gapless Wannier bands for the 2D SSH model. (b) The gapless Wannier bands for the 2D crossed SSH model. The model parameters are the same as those used for Fig. 3(b).

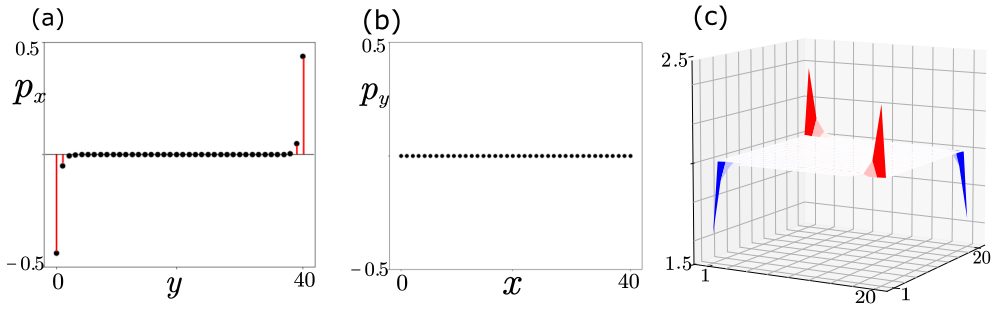

FIG. 7. (a, b) The numerical calculations of edge polarizations (p_x^{edge}, p_y^{edge}) for the second-order topological phase in case (iii). (c) The charge density distribution of the second-order topological insulator phase in the 2D crossed SSH model. The red and blue regions correspond to the positive and negative corner charge distribution, respectively. Here, we add the perturbations $0.001\tau_z\sigma_z$ to shift the energy of the corner states. We take the parameters as $t_x = 0.1$, $\lambda_x = 0.2$, $t_y = 0.3$, $\lambda_y = 1$ for (a–c).

$$|\Psi^{\text{g}}(x, k_y)\rangle_{z_x} = f_{z_x}^{\text{g}}(x) P_{z_x}^{\text{g}} |\psi^{\text{g}}(k_y)\rangle,$$
$$h_y^{\text{g}}(k_y)|\psi^{\text{g}}(k_y)\rangle = E_y(k_y)|\psi^{\text{g}}(k_y)\rangle, \tag{D9}$$

with the projection operators $P_{z_x}^{\text{g}} = (1 + z_x C_x^{\text{g}})/2$ and $P_{z_y}^{\text{g}} = (1 + z_y C_y^{\text{g}})/2$. It can be readily verified that

$$\mathcal{H}(k_x, y)|\Psi^{\text{g}}(k_x, y)\rangle_{z_y} = E_x(k_x)|\Psi^{\text{g}}(k_x, y)\rangle_{z_y},$$
$$\mathcal{H}(x, k_y)|\Psi^{\text{g}}(x, k_y)\rangle_{z_x} = E_y(k_y)|\Psi^{\text{g}}(x, k_y)\rangle_{z_x}, \tag{D10}$$

which means that the edge states $|\Psi^{\text{g}}(k_x, y)\rangle_{z_y}$ and $|\Psi^{\text{g}}(x, k_y)\rangle_{z_x}$ have the same energy spectrums as h_x and h_y, respectively.

Notably, the existence of the edge states along k_x and k_y requires $[C_y^{\text{g}}, h_x^{\text{g}}] = 0$ and $[C_x^{\text{g}}, h_y^{\text{g}}] = 0$, respectively. Otherwise, $|\Psi^{\text{g}}(k_x, y)\rangle_{z_y}$ or $|\Psi^{\text{g}}(k_y, x)\rangle_{z_x}$ is a null vector after the projection. It can be readily verified that $[C_x^{\text{i,ii}}, h_y] = 0$, $[C_y^{\text{i,ii}}, h_x] = 0$ for both cases (i) and (ii), and $\{C_x^{\text{iii}}, h_y\} = 0$, $[C_y^{\text{iii}}, h_x] = 0$ for case (iii). Therefore, there are both edge states along k_x and k_y for cases (i, ii), but there are edge states only along k_x for case (iii), as shown in Figs. 8(e) and 8(f). Correspondingly, the edge Hamiltonian describing these edge states can be obtained by projecting h_x or h_y into the subspace defined by P_{z_y} or P_{z_x}. Then we will find that these edge states are described by the two-band SSH model, which is consistent with the existence of edge isolated atoms coupled in a dimerized way in the limit case $t_x = t_y = 0$, as shown in Figs. 4(e)–(g).

Remarkably, the existence of edge states along k_x and k_y require that h_y and h_x are topologically nontrivial, respectively. Thus, the edge winding number $\tilde{\nu}_x = 1$ or $\tilde{\nu}_y = 1$ of the 1D edge states can completely reflect the CZESs existing conditions $\nu_x = \nu_y = 1$. As a result, the edge winding number can completely characterize the existence of the CZESs for cases (i–iii), revealing the unified edge-corner correspondence.

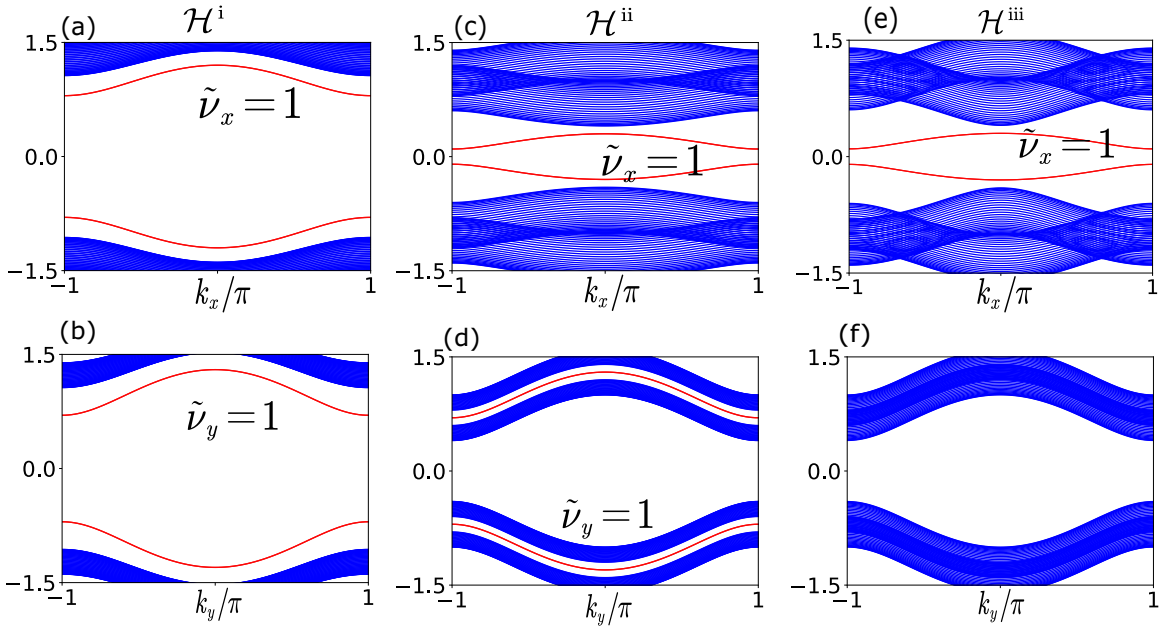

FIG. 8. (a, b) The energy spectrum for $\mathcal{H}^{\text{i}}(\boldsymbol{k})$ with ribbon geometry along the k_x and k_y directions, respectively. We take model parameters as $\lambda_x = \lambda_y = 1$, $t_x = 0.2$, $t_y = 0.3$. (c, d) The energy spectrum for $\mathcal{H}^{\text{ii}}(\boldsymbol{k})$ with ribbon geometry along the k_x and k_y directions, respectively. We take model parameters as $\lambda_x = 0.2$, $\lambda_y = 1$, $t_x = 0.1$, $t_y = 0.3$. (e, f) The energy spectrum for $\mathcal{H}^{\text{iii}}(\boldsymbol{k})$ with ribbon geometry along the k_x and k_y directions, respectively. We take model parameters as $\lambda_x = 0.2$, $\lambda_y = 1$, $t_x = 0.1$, $t_y = 0.3$.

APPENDIX E: THE CZESS IN THE SUPERCONDUCTING SYSTEM

In the superconducting Bogoliubov-de Gennes (BdG) basis $\Psi(\boldsymbol{k}) = (c_{\uparrow,\boldsymbol{k}}, c_{\downarrow,\boldsymbol{k}}, c^{\dagger}_{\uparrow,\boldsymbol{k}}, c^{\dagger}_{\downarrow,\boldsymbol{k}})$, we consider the superconductor BdG Hamiltonian

$$H_{\mathrm{BdG}} = \sum_{s=x,y} M_s(k_s)\Gamma^a_s + \lambda_s \sin k_s \Gamma^b_s, \tag{E1}$$

with the particle-hole symmetry $\mathcal{P} = \rho_x K$ and ρ the Pauli matrix in the particle-hole space. Restricted to the particle-hole symmetry, we have

$$\begin{aligned}\Gamma^a_x, \Gamma^a_y &\in \{\rho_z s_0, \rho_z s_x, \rho_z s_z, \rho_0 s_y, \rho_y s_y, \rho_x s_y\},\\ \Gamma^b_x, \Gamma^b_y &\in \{\rho_0 s_x, \rho_0 s_z, \rho_z s_y, \rho_x s_0, \rho_x s_z,\\ &\quad \rho_x s_x, \rho_y s_0, \rho_y s_x, \rho_y s_z\}.\end{aligned} \tag{E2}$$

with s the Pauli matrices in the spin space. Under the CZESs existing condition $[i\Gamma^a_x\Gamma^b_x, i\Gamma^a_y\Gamma^b_y] = 0$ for the Hamiltonian $\mathcal{H}_{\mathrm{BdG}}$, we will show that all four types of commutation relations listed in Eq. (7) can be realized.

For case (i), we require $\{\Gamma^a_x, \Gamma^{a,b}_y\} = 0, \{\Gamma^b_x, \Gamma^{a,b}_y\} = 0$. This case can be realized by considering the following six kinds of possible representations:

$$\begin{aligned}
&(1)\quad \Gamma^a_x = \rho_z s_x, \Gamma^b_x = \rho_y s_x, \Gamma^a_y = \rho_0 s_y, \Gamma^b_y = \rho_x s_x,\\
&(2)\quad \Gamma^a_x = \rho_z s_x, \Gamma^b_x = \rho_x s_0, \Gamma^a_y = \rho_z s_z, \Gamma^b_y = \rho_y s_0,\\
&(3)\quad \Gamma^a_x = \rho_y s_y, \Gamma^b_x = \rho_0 s_x, \Gamma^a_y = \rho_x s_y, \Gamma^b_y = \rho_z s_y,\\
&(4)\quad \Gamma^a_x = \rho_z s_0, \Gamma^b_x = \rho_x s_z, \Gamma^a_y = \rho_x s_y, \Gamma^b_y = \rho_y s_0,\\
&(5)\quad \Gamma^a_x = \rho_z s_0, \Gamma^b_x = \rho_x s_0, \Gamma^a_y = \rho_y s_y, \Gamma^b_y = \rho_y s_x,\\
&(6)\quad \Gamma^a_x = \rho_z s_z, \Gamma^b_x = \rho_0 s_x, \Gamma^a_y = \rho_0 s_y, \Gamma^b_y = \rho_x s_z.
\end{aligned} \tag{E3}$$

The Hamiltonians with the above Γ matrices representations are fully gapped and behave as second-order topological superconductors, which have completely identical topology properties to that of the BBH model. It is noted that the representations (1) and (2) in Eq. (E3) have been considered in references [88,89]. The realization of the model H_{BdG} with the Γ matrices representation (3) only needs the even parity pairings, which has been considered in reference [40]. Besides representation (3), the other representations require the p-wave pairings.

For case (ii), we require $[\Gamma^a_x, \Gamma^{a,b}_y] = 0, [\Gamma^b_x, \Gamma^{a,b}_y] = 0$. This case can be realized by considering the representation

$$\Gamma^a_x = \rho_z s_0,\ \Gamma^b_x = \rho_x s_x,\ \Gamma^a_y = \rho_z s_z,\ \Gamma^b_y = \rho_0 s_x. \tag{E4}$$

The realization of the model H_{BdG} with the above Γ matrix representation requires the p-wave pairing.

For case (iii), we require $[\Gamma^a_x, \Gamma^{a,b}_y] = 0, \{\Gamma^b_x, \Gamma^{a,b}_y\} = 0$. This case can be realized by considering the following two kinds of possible representations

$$\begin{aligned}
&(1)\quad \Gamma^a_x = \rho_z s_x,\ \Gamma^b_x = \tau_y s_0,\ \Gamma^a_y = \rho_z s_0,\ \Gamma^b_y = \rho_x s_z,\\
&(2)\quad \Gamma^a_x = \rho_z s_x,\ \Gamma^b_x = \rho_z s_y,\ \Gamma^a_y = \rho_y s_y,\ \Gamma^b_y = \rho_0 s_x.
\end{aligned} \tag{E5}$$

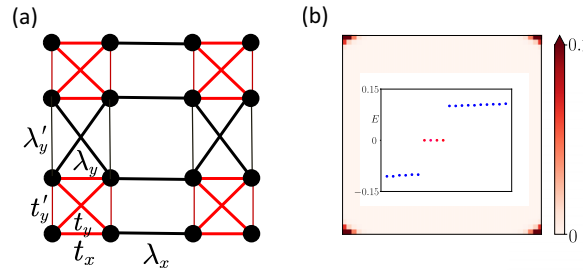

FIG. 9. (a) The 2D crossed SSH model with nearest-neighbor hopping (thin lines) along the y direction. The corner states of the 2D crossed SSH model with nearest-neighbor hopping. The inset shows the eigenenergies close to zero which are not symmetric about zero energy owing to the broken of the bulk chiral symmetry. We take the model parameters as $\lambda_x = t'_y = 0.2, t_x = \lambda'_y = 0.1, \lambda_y = 1, t_y = 0.3$.

The realization of the model H_{BdG} with the Γ matrices representation (1) needs the p-wave pairing. The realization of the model H_{BdG} with the Γ matrices representation (2) only needs the even parity pairing.

For case (iv), we require $[\Gamma^a_x, \Gamma^a_y] = 0, \{\Gamma^a_x, \Gamma^b_y\} = 0, \{\Gamma^b_x, \Gamma^a_y\} = 0, [\Gamma^b_x, \Gamma^b_y] = 0$. This case can be realized by considering the representation

$$\Gamma^a_x = \rho_z s_0,\ \Gamma^b_x = \rho_x s_z,\ \Gamma^a_y = \rho_z s_0,\ \Gamma^b_y = \rho_y s_x. \tag{E6}$$

The realization of the model H_{BdG} with the above Γ matrix representation needs the p-wave pairing.

APPENDIX F: 2D CROSSED SSH MODEL WITH THE NEAREST-NEIGHBOR HOPPING ALONG THE y DIRECTION

Based on the 2D crossed SSH model [Eq. (D1)], we consider the additional nearest-neighbor hopping along the y direction, represented by the thin lines in Fig. 9(a). These hoppings generates the addition terms $(t'_y + \lambda'_y \cos k_y)\tau_0\sigma_x$ and $\lambda'_y \sin k_y \tau_0\sigma_y$ to $\mathcal{H}^{\mathrm{iii}}$, which are also the two terms along the y direction of the 2D SSH model $\mathcal{H}^{\mathrm{ii}}$ [see Eq. (D1)].

Combining with Eqs. (D2) and (D3), we can find that the generated two terms break the bulk chiral symmetry $\mathcal{C}^{\mathrm{iii}} = -\tau_z\sigma_0$, but preserve the chiral symmetry $C^{\mathrm{iii}}_y = \tau_0\sigma_z$ of the 2D crossed SSH model. Although the bulk chiral symmetry is broken (the bulk energy spectrum is not symmetry about zero energy), the CZESs still exist, as shown in Fig. 9(b). This is because the CZESs are also protected by C^{iii}_y as

$$\langle\Psi_{z_x,z_y}|h_p|\Psi_{z_x,z_y}\rangle, = z_y\langle\Psi_{z_x,z_y}|\left(C^{\mathrm{iii}}_y h_p + h_p C^{\mathrm{iii}}_y\right)/2|\Psi_{z_x,z_y}\rangle = 0. \tag{F1}$$

Here h_p denotes the perturbation preserves C^{iii}_y with $\{h_p, C^{\mathrm{iii}}_y\} = 0$, $|\Psi_{z_x,z_y}\rangle$ denotes the CZES labeled by the eigenvalues z_x (z_y) of C^{iii}_x (C^{iii}_y). Therefore, a small nearest-neighbor hopping in the y direction cannot destroy the CZESs and is not important for realizing the 2D crossed SSH model.

[1] W. A. Benalcazar, B. A. Bernevig, and T. L. Hughes, Quantized electric multipole insulators, Science **357**, 61 (2017).

[2] W. A. Benalcazar, B. A. Bernevig, and T. L. Hughes, Electric multipole moments, topological multipole moment pumping, and chiral hinge states in crystalline insulators, Phys. Rev. B **96**, 245115 (2017).

[3] Z. Song, Z. Fang, and C. Fang, $(d-2)$-Dimensional Edge States of Rotation Symmetry Protected Topological States, Phys. Rev. Lett. **119**, 246402 (2017).

[4] J. Langbehn, Y. Peng, L. Trifunovic, F. von Oppen, and P. W. Brouwer, Reflection-Symmetric Second-Order Topological Insulators and Superconductors, Phys. Rev. Lett. **119**, 246401 (2017).

[5] F. Schindler, A. M. Cook, M. G. Vergniory, Z. Wang, S. S. P. Parkin, B. A. Bernevig, and T. Neupert, Higher-order topological insulators, Sci. Adv. **4**, eaat0346 (2018).

[6] M. Geier, L. Trifunovic, M. Hoskam, and P. W. Brouwer, Second-order topological insulators and superconductors with an order-two crystalline symmetry, Phys. Rev. B **97**, 205135 (2018).

[7] F. Schindler, Z. Wang, M. G. Vergniory, A. M. Cook, A. Murani, S. Sengupta, A. Yu. Kasumov, R. Deblock, S. Jeon, I. Drozdov, H. Bouchiat, S. Guéron, A. Yazdani, B. A. Bernevig, and T. Neupert, Higher-order topology in bismuth, Nat. Phys. **14**, 918 (2018).

[8] E. Khalaf, Higher-order topological insulators and superconductors protected by inversion symmetry, Phys. Rev. B **97**, 205136 (2018).

[9] B.-Y. Xie, H.-F. Wang, H.-X. Wang, X.-Y. Zhu, J.-H. Jiang, M.-H. Lu, and Y.-F. Chen, Second-order photonic topological insulator with corner states, Phys. Rev. B **98**, 205147 (2018).

[10] M. Serra-Garcia, V. Peri, R. Süsstrunk, O. R. Bilal, T. Larsen, L. G. Villanueva, and S. D. Huber, Observation of a phononic quadrupole topological insulator, Nature **555**, 342 (2018).

[11] B.-Y. Xie, G.-X. Su, H.-F. Wang, H. Su, X.-P. Shen, P. Zhan, M.-H. Lu, Z.-L. Wang, and Y.-F. Chen, Visualization of Higher-Order Topological Insulating Phases in Two-Dimensional Dielectric Photonic Crystals, Phys. Rev. Lett. **122**, 233903 (2019).

[12] X.-D. Chen, W.-M. Deng, F.-L. Shi, F.-L. Zhao, M. Chen, and J.-W. Dong, Direct Observation of Corner States in Second-Order Topological Photonic Crystal Slabs, Phys. Rev. Lett. **122**, 233902 (2019).

[13] X. Ni, M. Weiner, A. Alù, and A. B. Khanikaev, Observation of higher-order topological acoustic states protected by generalized chiral symmetry, Nat. Mater. **18**, 113 (2019).

[14] H. Fan, B. Xia, L. Tong, S. Zheng, and D. Yu, Elastic Higher-Order Topological Insulator with Topologically Protected Corner States, Phys. Rev. Lett. **122**, 204301 (2019).

[15] H. Xue, Y. Yang, G. Liu, F. Gao, Y. Chong, and B. Zhang, Realization of an Acoustic Third-Order Topological Insulator, Phys. Rev. Lett. **122**, 244301 (2019).

[16] M. Rodriguez-Vega, A. Kumar, and B. Seradjeh, Higher-order Floquet topological phases with corner and bulk bound states, Phys. Rev. B **100**, 085138 (2019).

[17] T. Nag, V. Juricić, and B. Roy, Out of equilibrium higher-order topological insulator: Floquet engineering and quench dynamics, Phys. Rev. Res. **1**, 032045(R) (2019).

[18] Y. Peng and G. Refael, Floquet Second-Order Topological Insulators from Nonsymmorphic Space-Time Symmetries, Phys. Rev. Lett. **123**, 016806 (2019).

[19] Y. Peng, Floquet higher-order topological insulators and superconductors with space-time symmetries, Phys. Rev. Res. **2**, 013124 (2020).

[20] H. Hu, B. Huang, E. Zhao, and W. V. Liu, Dynamical Singularities of Floquet Higher-Order Topological Insulators, Phys. Rev. Lett. **124**, 057001 (2020).

[21] B. Huang and W. V. Liu, Floquet Higher-Order Topological Insulators with Anomalous Dynamical Polarization, Phys. Rev. Lett. **124**, 216601 (2020).

[22] T. Nag, V. Juricić, and B. Roy, Hierarchy of higher-order Floquet topological phases in three dimensions, Phys. Rev. B **103**, 115308 (2021).

[23] A. K. Ghosh, T. Nag, and A. Saha, Floquet generation of a second-order topological superconductor, Phys. Rev. B **103**, 045424 (2021).

[24] T. Liu, Y.-R. Zhang, Q. Ai, Z. Gong, K. Kawabata, M. Ueda, and F. Nori, Second-Order Topological Phases in Non-Hermitian Systems, Phys. Rev. Lett. **122**, 076801 (2019).

[25] Z. Zhang, M. Rosendo López, Y. Cheng, X. Liu, and J. Christensen, Non-Hermitian Sonic Second-Order Topological Insulator, Phys. Rev. Lett. **122**, 195501 (2019).

[26] X.-W. Luo and C. Zhang, Higher-Order Topological Corner States Induced by Gain and Loss, Phys. Rev. Lett. **123**, 073601 (2019).

[27] E. Edvardsson, F. K. Kunst, and E. J. Bergholtz, Non-Hermitian extensions of higher-order topological phases and their biorthogonal bulk-boundary correspondence, Phys. Rev. B **99**, 081302(R) (2019).

[28] K. Kawabata, M. Sato, and K. Shiozaki, Higher-order non-Hermitian skin effect, Phys. Rev. B **102**, 205118 (2020).

[29] D. Varjas, A. Lau, K. Pöyhönen, A. R. Akhmerov, D. I. Pikulin, and I. C. Fulga, Topological Phases without Crystalline Counterparts, Phys. Rev. Lett. **123**, 196401 (2019).

[30] R. Chen, C.-Z. Chen, J.-H. Gao, B. Zhou, and D.-H. Xu, Higher-Order Topological Insulators in Quasicrystals, Phys. Rev. Lett. **124**, 036803 (2020).

[31] C.-B. Hua, R. Chen, B. Zhou, and D.-H. Xu, Higher-order topological insulator in a dodecagonal quasicrystal, Phys. Rev. B **102**, 241102(R) (2020).

[32] S. Spurrier and N. R. Cooper, Kane-mele with a twist: Quasicrystalline higher-order topological insulators with fractional mass kinks, Phys. Rev. Res. **2**, 033071 (2020).

[33] B. Lv, R. Chen, R. Li, C. Guan, B. Zhou, G. Dong, C. Zhao, Y. Li, Y. Wang, H. Tao, J. Shi, and D.-H. Xu, Realization of quasicrystalline quadrupole topological insulators in electrical circuits, Commun. Phys. **4**, 108 (2021).

[34] K. Wang, J.-X. Dai, L. B. Shao, S. A. Yang, and Y. X. Zhao, Boundary Criticality of $\mathcal{PT}$-Invariant Topology and Second-Order Nodal-Line Semimetals, Phys. Rev. Lett. **125**, 126403 (2020).

[35] C.-A. Li, B. Fu, Z.-A. Hu, J. Li, and S.-Q. Shen, Topological Phase Transitions in Disordered Electric Quadrupole Insulators, Phys. Rev. Lett. **125**, 166801 (2020).

[36] B. Liu, L. Xian, H. Mu, G. Zhao, Z. Liu, A. Rubio, and Z. F. Wang, Higher-Order Band Topology in Twisted Moiré Superlattice, Phys. Rev. Lett. **126**, 066401 (2021).

[37] C.-A. Li, S.-B. Zhang, J. Li, and B. Trauzettel, Higher-Order Fabry-Pérot Interferometer from Topological Hinge States, Phys. Rev. Lett. **127**, 026803 (2021).

[38] P.-L. Zhao, X.-B. Qiang, H.-Z. Lu, and X. C. Xie, Coulomb Instabilities of a Three-Dimensional Higher-Order Topological Insulator, Phys. Rev. Lett. **127**, 176601 (2021).

[39] Y.-T. Hsu, W. S. Cole, R.-X. Zhang, and J. D. Sau, Inversion-Protected Higher-Order Topological Superconductivity in Monolayer WTe_2, Phys. Rev. Lett. **125**, 097001 (2020).

[40] M. Kheirkhah, Z. Yan, Y. Nagai, and F. Marsiglio, First- and Second-Order Topological Superconductivity and Temperature-Driven Topological Phase Transitions in the Extended Hubbard Model with Spin-Orbit Coupling, Phys. Rev. Lett. **125**, 017001 (2020).

[41] R.-X. Zhang and S. Das Sarma, Intrinsic Time-Reversal-Invariant Topological Superconductivity in Thin Films of Iron-Based Superconductors, Phys. Rev. Lett. **126**, 137001 (2021).

[42] X.-J. Luo, X.-H. Pan, and X. Liu, Higher-order topological superconductors based on weak topological insulators, Phys. Rev. B **104**, 104510 (2021).

[43] A. K. Ghosh, T. Nag, and A. Saha, Hierarchy of higher-order topological superconductors in three dimensions, Phys. Rev. B **104**, 134508 (2021).

[44] X.-H. Pan, X.-J. Luo, J.-H. Gao, and X. Liu, Detecting and braiding higher-order Majorana corner states through their spin degree of freedom, Phys. Rev. B **105**, 195106 (2022).

[45] Y. Tan, Z.-H. Huang, and X.-J. Liu, Two-particle Berry phase mechanism for Dirac and Majorana Kramers pairs of corner modes, Phys. Rev. B **105**, L041105 (2022).

[46] T. E. Pahomi, M. Sigrist, and A. A. Soluyanov, Braiding Majorana corner modes in a second-order topological superconductor, Phys. Rev. Res. **2**, 032068(R) (2020).

[47] S.-B. Zhang, W. B. Rui, A. Calzona, S.-J. Choi, A. P. Schnyder, and B. Trauzettel, Topological and holonomic quantum computation based on second-order topological superconductors, Phys. Rev. Res. **2**, 043025 (2020).

[48] S.-B. Zhang, A. Calzona, and B. Trauzettel, All-electrically tunable networks of Majorana bound states, Phys. Rev. B **102**, 100503(R) (2020).

[49] C. Nayak, S. H. Simon, A. Stern, M. Freedman, and S. Das Sarma, Non-Abelian anyons and topological quantum computation, Rev. Mod. Phys. **80**, 1083 (2008).

[50] Y. Wu, H. Jiang, J. Liu, H. Liu, and X. C. Xie, Non-Abelian Braiding of Dirac Fermionic Modes Using Topological Corner States in Higher-Order Topological Insulator, Phys. Rev. Lett. **125**, 036801 (2020).

[51] Z. Yan, F. Song, and Z. Wang, Majorana Corner Modes in a High-Temperature Platform, Phys. Rev. Lett. **121**, 096803 (2018).

[52] C.-H. Hsu, P. Stano, J. Klinovaja, and D. Loss, Majorana Kramers Pairs in Higher-Order Topological Insulators, Phys. Rev. Lett. **121**, 196801 (2018).

[53] Q. Wang, C.-C. Liu, Y.-M. Lu, and F. Zhang, High-Temperature Majorana Corner States, Phys. Rev. Lett. **121**, 186801 (2018).

[54] X.-L. Sheng, C. Chen, H. Liu, Z. Chen, Z.-M. Yu, Y. X. Zhao, and S. A. Yang, Two-Dimensional Second-Order Topological Insulator in Graphdiyne, Phys. Rev. Lett. **123**, 256402 (2019).

[55] X.-H. Pan, K.-J. Yang, L. Chen, G. Xu, C.-X. Liu, and X. Liu, Lattice-Symmetry-Assisted Second-Order Topological Superconductors and Majorana Patterns, Phys. Rev. Lett. **123**, 156801 (2019).

[56] X. Zhu, Second-Order Topological Superconductors with Mixed Pairing, Phys. Rev. Lett. **122**, 236401 (2019).

[57] Y. Volpez, D. Loss, and J. Klinovaja, Second-Order Topological Superconductivity in π-Junction Rashba Layers, Phys. Rev. Lett. **122**, 126402 (2019).

[58] R.-X. Zhang, W. S. Cole, and S. Das Sarma, Helical Hinge Majorana Modes in Iron-Based Superconductors, Phys. Rev. Lett. **122**, 187001 (2019).

[59] Y. Ren, Z. Qiao, and Q. Niu, Engineering Corner States from Two-Dimensional Topological Insulators, Phys. Rev. Lett. **124**, 166804 (2020).

[60] Y.-J. Wu, J. Hou, Y.-M. Li, X.-W. Luo, X. Shi, and C. Zhang, In-plane Zeeman-Field-Induced Majorana Corner and Hinge Modes in an s-Wave Superconductor Heterostructure, Phys. Rev. Lett. **124**, 227001 (2020).

[61] X. Wu, W. A. Benalcazar, Y. Li, R. Thomale, C.-X. Liu, and J. Hu, Boundary-Obstructed Topological High-t_c Superconductivity in Iron Pnictides, Phys. Rev. X **10**, 041014 (2020).

[62] C. Chen, Z. Song, J.-Z. Zhao, Z. Chen, Z.-M. Yu, X.-L. Sheng, and S. A. Yang, Universal Approach to Magnetic Second-Order Topological Insulator, Phys. Rev. Lett. **125**, 056402 (2020).

[63] L. Chen, B. Liu, G. Xu, and X. Liu, Lattice distortion induced first- and second-order topological phase transition in a rectangular high-T_c superconducting monolayer, Phys. Rev. Res. **3**, 023166 (2021).

[64] F. Liu and K. Wakabayashi, Novel Topological Phase with a Zero Berry Curvature, Phys. Rev. Lett. **118**, 076803 (2017).

[65] B. Kang, K. Shiozaki, and G. Y. Cho, Many-body order parameters for multipoles in solids, Phys. Rev. B **100**, 245134 (2019).

[66] W. A. Wheeler, L. K. Wagner, and T. L. Hughes, Many-body electric multipole operators in extended systems, Phys. Rev. B **100**, 245135 (2019).

[67] S. Ono, L. Trifunovic, and H. Watanabe, Difficulties in operator-based formulation of the bulk quadrupole moment, Phys. Rev. B **100**, 245133 (2019).

[68] W. A. Benalcazar and A. Cerjan, Bound states in the continuum of higher-order topological insulators, Phys. Rev. B **101**, 161116(R) (2020).

[69] M. Jung, Y. Yu, and G. Shvets, Exact higher-order bulk-boundary correspondence of corner-localized states, Phys. Rev. B **104**, 195437 (2021).

[70] W. P. Su, J. R. Schrieffer, and A. J. Heeger, Solitons in Polyacetylene, Phys. Rev. Lett. **42**, 1698 (1979).

[71] M. Ezawa, Edge-corner correspondence: Boundary-obstructed topological phases with chiral symmetry, Phys. Rev. B **102**, 121405(R) (2020).

[72] L. Trifunovic, Bulk-and-edge to corner correspondence, Phys. Rev. Res. **2**, 043012 (2020).

[73] Y.-S. Hu, Y.-R. Ding, J. Zhang, Z.-Q. Zhang, and C.-Z. Chen, Disorder and phase diagrams of higher-order topological insulators, Phys. Rev. B **104**, 094201 (2021).

[74] B. A. Bernevig, T. L. Hughes, and S.-C. Zhang, Quantum spin hall effect and topological phase transition in HGTE quantum wells, Science **314**, 1757 (2006).

[75] L. Trifunovic and P. W. Brouwer, Higher-Order Bulk-Boundary Correspondence for Topological Crystalline Phases, Phys. Rev. X **9**, 011012 (2019).

[76] W. A. Benalcazar, T. Li, and T. L. Hughes, Quantization of fractional corner charge in C_n-symmetric higher-order topological crystalline insulators, Phys. Rev. B **99**, 245151 (2019).

[77] J. Bao, D. Zou, W. Zhang, W. He, H. Sun, and X. Zhang, Topoelectrical circuit octupole insulator with topologically protected corner states, Phys. Rev. B **100**, 201406(R) (2019).

[78] Z. Yan, Higher-Order Topological Odd-Parity Superconductors, Phys. Rev. Lett. **123**, 177001 (2019).

[79] W. Zhang, D. Zou, J. Bao, W. He, Q. Pei, H. Sun, and X. Zhang, Topolectrical-circuit realization of a four-dimensional hexadecapole insulator, Phys. Rev. B **102**, 100102(R) (2020).

[80] E. Khalaf, W. A. Benalcazar, T. L. Hughes, and R. Queiroz, Boundary-obstructed topological phases, Phys. Rev. Res. **3**, 013239 (2021).

[81] R. W. Bomantara, L. Zhou, J. Pan, and J. Gong, Coupled-wire construction of static and Floquet second-order topological insulators, Phys. Rev. B **99**, 045441 (2019).

[82] M. Serra-Garcia, R. Süsstrunk, and S. D. Huber, Observation of quadrupole transitions and edge mode topology in an LC circuit network, Phys. Rev. B **99**, 020304(R) (2019).

[83] S. Imhof, C. Berger, F. Bayer, J. Brehm, L. W. Molenkamp, T. Kiessling, F. Schindler, C. H. Lee, M. Greiter, T. Neupert, and R. Thomale, Topolectrical-circuit realization of topological corner modes, Nat. Phys. **14**, 925 (2018).

[84] S. Mittal, V. V. Orre, G. Zhu, M. A. Gorlach, A. Poddubny, and M. Hafezi, Photonic quadrupole topological phases, Nat. Photon. **13**, 692 (2019).

[85] L.-Y. Zheng, V. Achilleos, O. Richoux, G. Theocharis, and V. Pagneux, Observation of Edge Waves in a Two-Dimensional Su-Schrieffer-Heeger Acoustic Network, Phys. Rev. Appl. **12**, 034014 (2019).

[86] Y. Qi, C. Qiu, M. Xiao, H. He, M. Ke, and Z. Liu, Acoustic Realization of Quadrupole Topological Insulators, Phys. Rev. Lett. **124**, 206601 (2020).

[87] L. Zhang, L. Zhang, S. Niu, and X.-J. Liu, Dynamical classification of topological quantum phases, Sci. Bull. **63**, 1385 (2018).

[88] Y. Wang, M. Lin, and T. L. Hughes, Weak-pairing higher order topological superconductors, Phys. Rev. B **98**, 165144 (2018).

[89] A. Tiwari, A. Jahin, and Y. Wang, Chiral Dirac superconductors: Second-order and boundary-obstructed topology, Phys. Rev. Res. **2**, 043300 (2020).